ANALYSIS
of
THIN TRIANGULAR CONDUCTING ELEMENTS PRINTED on PLANAR DIELECTRIC SLABS

M.Sc. Thesis
in
Electrical and Electronics Engineering
University of Gaziantep

Supervisor
Prof. Dr. Tuncay EGE

by

Ayşegül Pekmezci

January 2010

T.C.
UNIVERSITY OF GAZİANTEP
GRADUATE SCHOOL OF
NATURAL & APPLIED SCIENCES
ELECTRICAL&ELECTRONICS ENGINEERING

Name of the thesis : Analysis of Thin Triangular Conducting Elements Printed on Planar Dielectric Slabs

Name of the student: Ayşegül Pekmezci
Exam date : 12.01.2010

Approval of the Graduate School of Natural and Applied Sciences

Prof. Dr. Ramazan KOÇ
Director

I certify that this thesis satisfies all the requirements as a thesis for the degree of Master of Science.

Prof. Dr. Savaş UÇKUN
Head of Department

This is to certify that we have read this thesis and that in our opinion it is fully adequate, in scope and quality, as a thesis for the degree of Master of Science.

Prof. Dr. Tuncay EGE
Supervisor

Examining Committee Members	signature
Prof. Dr. Savaş UÇKUN.....	_____
Prof. Dr. Tuncay EGE.....	_____
Prof. Dr. Sadettin ÖZYAZICI.....	_____
Prof. Dr. L. Canan DÜLGER.....	_____
Y.Doç. Gölge ÖĞÜCÜ….....	_____

ABSTRACT

ANALYSIS of THIN TRIANGULAR CONDUCTING ELEMENTS PRINTED on PLANAR DIELECTRIC SLABS

PEKMEZCİ Ayşegül
M.Sc. in Electrical and Electronics Engineering
Supervisor: Prof. Dr. Tuncay EGE
January 2010, 56 pages

In this study, scattering characteristics of thin triangular conducting elements periodically printed on planar dielectric slabs are investigated theoretically for transverse electric (TE) and transverse magnetic (TM) incident plane waves. Such surfaces are known as frequency selective surfaces (FSS) and they show bandpass or stop band filter characteristics.

Since the conducting elements are etched periodically on such a surface, all fields and currents must satisfy Floquet's condition and should be written as Floquet modes. Using Floquet's theorem and satisfying the required boundary conditions, an integral equation is obtained for the unknown induced current density on the surface of a triangular conducting element in a unit cell. This current is then expressed as a finite sum of piecewise triangular basis functions having unknown coefficients. The resulting integral equation is then converted to a linear matrix equation by using the Moment Method (MM) and inversion of the matrix equation yields the unknown current coefficients which are used to obtain the reflection and transmission coefficients.

Numerical results for the reflection and transmission coefficients are then plotted versus frequency for freestanding and dielectric backed triangular-shaped FSS elements. Furthermore, the variation of reflection characteristics with dielectric constant (ε_r), slab thickness (t), length and width of the triangle ($L_{1,2,3}, w$), incidence angle (θ) and lattice dimensions ($d_{x,y}$) are presented in the form of graphs.

Key words: Triangular Conducting Elements, Frequency Selective Surfaces, Moment Method

ÖZET

DÜZLEMSEL DİELEKTRİK LEVHA ÜZERİNE YERLEŞTİRİLMİŞ İNCE ÜÇGEN YAPILI İLETKEN ELEMANLARIN ANALİZİ

PEKMEZCİ Ayşegül
Yüksek Lisans Tezi Elektrik Elektronik Mühendisliği Bölümü
Tez Yöneticisi: Prof. Dr. Tuncay EGE
Ocak 2010, 56 sayfa

Bu çalışmada düzlemsel dielektrik levha üzerine periyodik olarak yerleştirilmiş ince üçgen şeklindeki iletken elemanların levhaya dik gelen TM ve TE düzlem dalgaları için saçılma özellikleri incelenmiştir. Bu tür yüzeyler Frekans Seçici Yüzey (FSY) olarak adlandırılırlar ve bant geçirici ya da durdurucu filtre özelliği gösterirler.

Frekans Seçici Yüzey (FSY) üzerindeki iletken elemanlar periyodik olarak yerleştirildiklerinden dolayı, oluşan tüm alanlar ve akımlar Floquet şartlarını sağlamalıdır. Bu sebeple, dielektrik levha üzerine yerleştirilen iletken elemanların üzerinde indüklenen akımlar için Floquet Teoremi kullanılarak bir integral denklemi elde edilir. Daha sonra buradaki akımlar, sınırlı sayıdaki bilinmeyen katsayılı temel üçgen fonksiyonlarının toplamı olarak ifade edilirler. Elde edilen integral denklemi, iletim ve yansıma katsayılarının hesaplanmasında kullanılacak olan bilinmeyen akım katsayılarının bulunması için Moment Metodu aracılığıyla çözülür.

Havada asılı ve dielektrik levha üzerine yerleştirilmiş üçgen şekilli FSY elemanları için bulunan iletim ve yansıma katsayılarının frekansa göre grafikleri çizilmiş olup yansıma katsayısının frekansa göre değişimi, gelme açısı, levha kalınlığı, iletken elemanın uzunluğu gibi farklı parametre değerleri için de ayrıca gösterilmiştir.
Sonuç olarak, önceki çalışmalarda da olduğu gibi üçgen şekilli FSY'lerin de bant durdurucu özelliği olduğu gözlemlenmiş ve benzerlikler ifade edilmiştir.

Anahtar kelimeler: Üçgen Yapılı İletken Elemanlar, Frekans Seçici Yüzeyler, Moment Metot

ACKNOWLEDGEMENTS

I would like to express my sincerest gratitude to the perfect teacher and supervisor Prof. Dr. Tuncay Ege for his guidance, suggestions and great help in the preparation of the theory and some mathematical software for numerical analysis.

I also thank my family for their love, advice and encouragements.

TABLE of CONTENTS

LIST of FIGURES

CHAPTER 1

INTRODUCTION

1.1 Introduction

Frequency selective surface (FSS) is a surface which exhibits different reflection and transmission properties as a function of frequency. These surfaces are usually constructed from periodically arranged metallic patches of arbitrary geometries or their complementary geometry having aperture elements similar to patches within a metallic screen. The shape and configurations of the geometry for FSSs depends on the imagination of the researcher.

As the metallic patches are arranged periodically in air or a dielectric substrate, FSS shows total reflection properties (reflects nearly all energy) at some specific frequency called the resonance frequency whereas in the complimentary structures where the metallic screen is perforated, it transmits all energy (total transmission) at the resonance frequency. So, it is seen that aperture and patch screens generally yield give complementary frequency responses [1].

Choosing appropriate parameters also have a significant role in the design of desired FSS. The most important parameters in the design are the element geometry, the periodicity of the structure and the type of the dielectric substrate [1] which determine the overall frequency response of the structure such as; stability of the resonant frequency, bandwidth shape: narrow or broadband and rate of roll-off avoiding the higher order harmonics that cause grating lobes.

1.2 Typical Application

FSSs are incorporated in a wide variety of applications such as the realization of reflector antennas, radome designs, constructions of polarizers, beam splitters, and some kind of absorbers and photonic band gap structures.

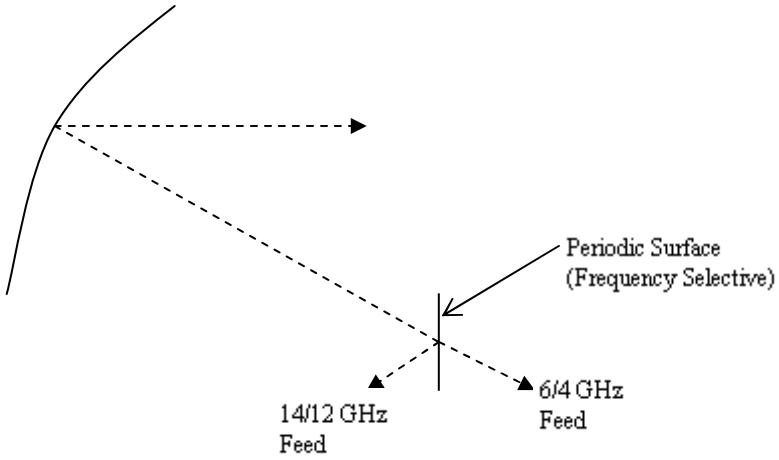

Figure1.1 Reflector antenna system using frequency selective screen

As shown in Figure1.1, a FSS is placed between two feeds radiating at different frequencies and the main reflector [2]. The screen is totally reflecting or totally transparent over the operating band of feed one and two, respectively. Hence, two independent feeds may share the same reflector antenna simultaneously.

The other application of FSS in microwave region is in radome design [2]. Radomes protect an antenna from the environment by tuning the screen at the operating frequency of the antenna to provide a bandpass transmission characteristic. At the out of band frequencies the screen can be made totally reflecting, and the radome can be designed to blend with the skin of the vehicle such that minimal scattering occurs at the joint between the radome and the skin.

In far-infrared region, the application of FSSs involves polarizers, beam splitters [2]. A polarizer can be constructed from a diffraction grating such that the fields polarized parallel to the grating are reflected, while those with an orthogonal

polarization are transmitted. An FSS comprising of meanderlines can be used as a polarizer to convert a linearly polarized wave into a circularly polarized one [1].

In the near-infrared and visible portions of the spectrum, periodic screens have been also proposed as solar selective surfaces to aid in the collection of solar energy [2]. A screen is designed such that it is essentially transparent in the frequency band where the solar cells are most efficient and is reflecting at frequencies outside this band.

When the photonic bandgap structures are used in applications of FSSs, the designer could extend the frequency selective screen by periodically adding many layers in the third dimension [1]. For this reason, the photonic bandgap material consists of three-dimensional periodic structures that exhibit spectral bands where all propagation is prohibited at any incident angle and for any polarization.

Circuit analog absorbers are the other applications of FSS which are made of periodic structures of very lossy material [3]. That kind of absorbers is designed to produce a larger bandwidth per given thickness, particularly as more layers are added.

1.3 Literature Summary

FSSs have been the subject of investigation by many researchers because of their various important applications.

The problem of scattering by a two-dimensional periodic array of rectangular plates was studied by Ott et al. [4] and the integral equation was solved for the unknown current on each plate by using the point matching method. Then the solution given is restricted to the case of narrow plates arranged in a rectangular lattice with a normally incident plane wave. The complementary problem of scattering by a conducting screen perforated periodically with apertures was analyzed by Kieburtz and Ishimaru [5] by the variational method.

In 1970, a more general formulation of the scattering problem for a two-dimensional periodic array of plates was presented by C.C.Chen [6]. The electromagnetic field distribution near the array of the conducting plates was expanded into a set of Floquet mode functions, and an integral equation for the unknown induced current was obtained. Then the coefficients of unknown current were determined by the method of moments.

In 1975, J.P.Montgomery [7] solved the problem of scattering of a plane wave by an infinite periodic array of thin conductors for unsymmetrical structures.

In 1979, a new analysis for calculating the scattering periodically arrays of symmetrical cross dipoles was presented by Pelton and Munk [8].

In 1981, Parker and Hamdy [9] pointed out that the arrays of simple rings can form useful FSSs for reflector antennas.

Tsao and Mittra presented a new technique, called the spectral-iteration approach, for analyzing the problem of scattering from periodically perforated screens in 1982 [10]. They obtained a set of algebraic equations for the spectral coefficients of the aperture field or the induced current. And then these equations were solved simultaneously using the iterative procedure developed by these authors. They also presented a full-wave analysis for FSSs comprised of periodic arrays of cross dipoles and Jeruselam crosses [11].

Tripoles were used originally by Pelton and Munk[12] as elements for slot arrays I metallic radomes. Then, in 1983, Vardaxoglou and Parker [13] investigated the performance of tripole arrays as FSS. They showed that the current distribution along the arms of tripoles arranged on two equilateral lattices.

There are also some other loop-type and plate-type structures such as circular, square, hexagonal that have been investigated as FSS up to now[3]. However, the FSSs comprised of L-shaped and one-turn helix shaped conductors were firstly studied by Delihacıoglu in his doctorial dissertation [14]. On the other hand,

Blinnikova et al. [15] considered the L-shaped apertures in FSSs for the first time in 2007.

When the literature is searched, we found that no study has been done on FSSs comprising of triangular-shaped conductors. That is why, in this study, we investigated the reflection and transmission characteristics of FSS formed by a two dimensional array of triangular shaped conductors printed on a dielectric substrate.

1.4 Method of This Work

Due to the periodicity of FSSs, the analysis is carried out in terms of infinite periodic structures and the formulation reduces to the investigation of one periodic unit cell which is identical to those in an adjacent cell differing only by the incident field phase shift. And this analysis is performed by applying Floquet's Theorem. So, an integral equation for the unknown current on each conducting element is obtained by enforcing the required boundary conditions on the conducting elements.

In order to solve this integral equation Moment Method (MM) has been widely used. By using MM [16] this integral equation is converted to a linear matrix equation of the form $(Z)i = V$. Here, (Z) is the impedance matrix, V is the known excitation function and i is the vector that contains the unknown coefficients of the basis functions. Taking the inverse transform of the matrix equation, the unknown current coefficients are obtained. Thus, choosing the proper basis function plays an important role to define the number of unknown induced currents which affect the size of the impedance matrix.

Introduction to Floquet's Theorem and Floquet Modes is given in Chapter 2 and a brief explanation of MM and the basis function adopted for our work is given in Chapter 3. Furthermore, in this chapter the triangular-shaped FSS backed by dielectric slab is formulated. The formulation is in the form of an integral equation in terms of the current induced on a scatterer in a unit cell. By using MM, this equation is solved for the induced current density on the triangular-shaped conductor and the reflection and transmission coefficients are then expressed in terms of the known

induced current distribution. In order to verify the correctness of the algorithm developed for the triangular-shaped conducting elements in this study, comparison with FSSs composed of conducting strips and L-dipoles are also given.

In Chapter 4, numerical results for the reflection and transmission characteristics are presented. For an FSS comprising of triangular conducting elements, all numerical results for the reflection and transmission coefficients are plotted versus frequency for freestanding and dielectric backed triangular-shaped FSS elements. Furthermore, the variation of reflection characteristics with dielectric constant (ε_r), slab thickness (t), length and width of the triangle ($L_{1,2,3}, w$), incidence angle (θ) and lattice dimensions ($d_{x,y}$) are presented in the form of graphs.

Finally, in Chapter 5 a discussion on the results obtained and the performance of the proposed FSS is presented.

CHAPTER 2

PERIODIC STRUCTURES AND FLOQUET'S THEOREM

2.1 Floquet's Theorem

Periodic structures such as arrays of conducting elements or periodically perforated screens which can be either freestanding or printed on dielectric substrates have frequency selective properties.

All the elements in the array, which is periodic and extends to the infinity in both x and y directions, are assumed to be identical, infinitesimally thin and perfectly conducting. This allows us to expand the scattered fields inside the dielectric slab and in the air on either side into a complete set of orthogonal modes known as Floquet modes [17, 18].

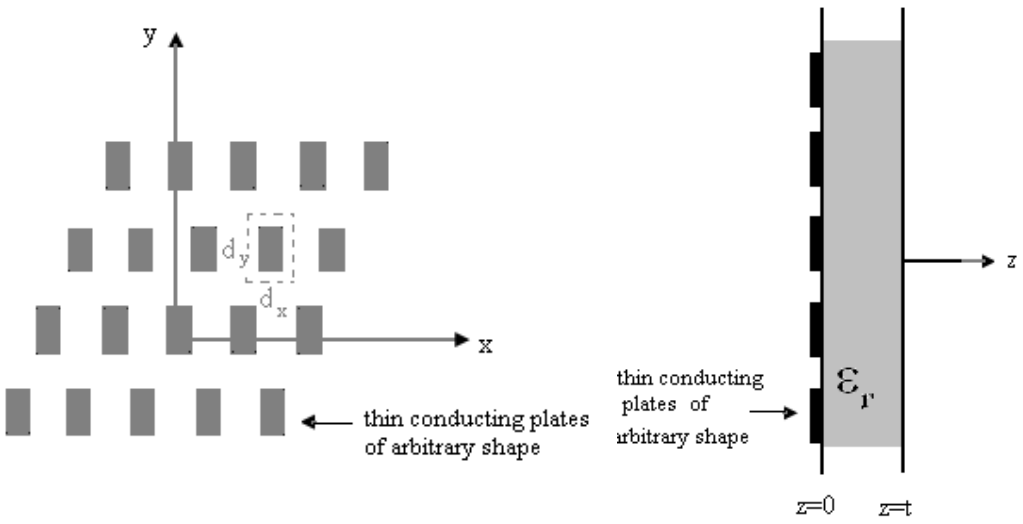

Figure 2.1 Arbitrary geometry of Frequency Selective Surface (a) Top view (b) Side view

In the cartesian coordinate system in unbounded space, a component of the electric field in the region ($z \geq 0$) is a solution of the scalar homogeneous Helmholtz equation.

$$(\nabla^2 + k^2)\Psi(x,y,z) = 0 \tag{2.1}$$

where

$$k^2 = k_x{}^2 + k_y{}^2 + \gamma^2$$

Assuming waves propagating in z direction, the variation of the field with z can be written as

$$\Psi(x,y,z) = e^{-j\gamma z}\Psi(x,y) \tag{2.2}$$

Then the equation (2.1) becomes

$$\left[\frac{\partial^2}{\partial x^2} + \frac{\partial^2}{\partial y^2} + (k^2 - \gamma^2)\right]\Psi(x,y) = 0 \tag{2.3}$$

The partial differential equation (2.3) can be converted into two ordinary differential equations by applying the technique of separation of variables. That is by assuming $\Psi(x,y) = f(x)g(y)$ we can write

$$\left[\frac{\partial^2}{\partial x^2} + \frac{\partial^2}{\partial y^2} + (k_x{}^2 + k_y{}^2)\right]f(x)g(y) = 0 \tag{2.4}$$

Then,

$$\left[\frac{d^2}{dx^2} + k_x{}^2\right]f(x) = 0 \tag{2.5}$$

$$\left[\frac{d^2}{dy^2} + k_y{}^2\right]g(y) = 0 \tag{2.6}$$

The solution of the equations (2.5) and (2.6) is $f(x) = e^{-jk_x x}$ for x dependence, and $g(y) = e^{-jk_y y}$ for y dependence, respectively.

Since the structure is periodic both in x and y directions, the solution of the equations 2.5 and 2.6 should also be periodic according to the Floquet theorem. Thus, the periodic form of f(x) and g(y), representing the waves propagating in x and y direction must satisfy the periodicity condition;

$$f(x+d_x) = e^{-jk_x d_x} f(x) \tag{2.7}$$

$$g(y+d_y) = e^{-jk_y d_y} g(y) \tag{2.8}$$

where

$$k_x = k\sin\theta\cos\phi$$

$$k_y = k\sin\theta\sin\phi$$

and d_x, d_y are the surface periodicities in the x and y directions respectively.

This is possible if,

$$f(x) = e^{-jk_x x} F_p(x) \tag{2.9}$$

$$g(y) = e^{-jk_y y} G_p(y) \tag{2.10}$$

where $F_p(x)$ and $G_p(y)$ are the periodic functions of x with a period d_x and y with a period of d_y, respectively. Therefore, $F_p(x)$ and $G_p(y)$ can be expanded into a Fourier series.

$$F_p(x) = \sum_{p=-\infty}^{\infty} A_p e^{-j\frac{2\pi}{d_x}px} \tag{2.11}$$

$$G_q(y) = \sum_{q=-\infty}^{\infty} B_q e^{-j\frac{2\pi}{d_y}qy} \tag{2.12}$$

Substituting 2.11 and 2.12 into 2.9 and 2.10, we can obtain;

$$f(x) = \sum_{p=-\infty}^{\infty} A_p e^{-j(k_x+\frac{2\pi p}{d_x})x} \tag{2.13}$$

$$g(y) = \sum_{q=-\infty}^{\infty} B_q e^{-j(k_y+\frac{2\pi q}{d_y})y} \tag{2.14}$$

where

$$k_{xp} = k_x + \frac{2\pi p}{d_x}, \qquad p = 0, \pm1, \pm2, ...$$

$$k_{yq} = k_y + \frac{2\pi q}{d_y}, \qquad q = 0, \pm1, \pm2, ...$$

Hence, in a source free region the solution to the scalar wave equation (2.2) can be written for z>0 as

$$\Psi(x,y,z)=\sum_{p=-\infty}^{\infty}\sum_{q=-\infty}^{\infty}C_{pq}e^{-j(k_x+\frac{2\pi p}{d_x})x}e^{-j(k_y+\frac{2\pi q}{d_y})y}e^{-j\gamma_{pq}z} \tag{2.15}$$

where

$$\gamma_{pq}{}^2=k^2-(k_x+\frac{2\pi p}{d_x})^2-(k_y+\frac{2\pi q}{d_y})^2 \tag{2.16}$$

The constants k_x and k_y are the wave numbers in the x and y directions of the incident wave and the indices of integers $\{p,q\}$ defines the location of the elements.

In the literature many authors treated periodic structures positioned along skewed coordinates [18]. In this case, the solution to the scalar wave equation (1.15) is given by the following equation.

$$\Psi(x,y,z)=\sum_{p=-\infty}^{\infty}\sum_{q=-\infty}^{\infty}C_{pq}e^{-j(k_x+\frac{2\pi p}{d_x})x}e^{-j(k_y+\frac{2\pi q}{d_y\sin\Omega}-\frac{2\pi p}{d_x\tan\Omega})y}e^{-j\gamma_{pq}z} \tag{2.17}$$

$$\Psi(x,y,z)=\sum_{p=-\infty}^{\infty}\sum_{q=-\infty}^{\infty}C_{pq}e^{-j\vec{K}_{Tpq}\bullet\vec{\rho}}e^{-j\gamma_{pq}z} \tag{2.18}$$

where

$$\vec{\rho}=x\vec{a}_x+y\vec{a}_y$$

$$\vec{K}_{Tpq}=(k_x+\frac{2\pi p}{d_x})\vec{a}_x+(k_y+\frac{2\pi q}{d_y\sin\Omega}-\frac{2\pi p}{d_x\tan\Omega})\vec{a}_y$$

$$\gamma_{pq}{}^2=k^2-\vec{K}_{Tpq}\bullet\vec{K}_{Tpq}$$

If the array geometry is made up of square cells, then choosing the angle Ω between the skew axes to be equal to 90° in (2.17) yields (2.15).

Here, the modal propagation constant γ_{pq} can be positive real for propagating modes or purely negative imaginary for evanescent modes depending on the linear phase variations of the incident field k_x, k_y and the integers p, q.

2.2 Analysis of FSS

In this section, a more general formulation of the scattering problem of a FSS printed on a single layer of dielectric is presented.

The traverse electric and magnetic fields inside and outside the dielectric layer is expanded into Floquet modes. The resultant TE and TM Floquet harmonics, transverse with respect to the z axis, are

$$\vec{\Psi}_{mpq}(x,y) = \frac{1}{\sqrt{A}} e^{-j\vec{K}_{Tpq}\bullet\vec{\rho}}\vec{u}_{mpq} \tag{2.19}$$

where

$A = d_x d_y$ (area of a unit cell)

$$\vec{K}_{Tpq} = (k_x + \frac{2\pi p}{d_x})\vec{a}_x + (k_y + \frac{2\pi q}{d_y})\vec{a}_y = k_{xpq}\vec{a}_x + k_{ypq}\vec{a}_y$$

$$\vec{\rho} = x\vec{a}_x + y\vec{a}_y$$

$$\vec{u}_{1pq} = \frac{\vec{K}_{Tpq}}{\left|\vec{K}_{Tpq}\right|} \quad , m = 1 \text{ for TM mode}$$

$$\vec{u}_{2pq} = a_z \times \vec{u}_{1pq} \quad , m = 2 \text{ for TE mode}$$

and

$p = q = 0, \pm 1, \pm 2, \ldots$

It is known that a plane wave can always be decomposed into a combination of E and H field that corresponds to the TM and TE Floquet modes with p=0, q=0. For this reason, in the absence of metallic scatterer but in the presence of the dielectric layer, the scattered fields contains only zero order Floquet modes.

So, the incident plane waves in the region $z \leq 0$ with the zero order TM and TE Floquet modes can be expressed as;

$$\vec{E}_{inc} = \frac{1}{\sqrt{A}} \sum_{m=1}^{2} A_{moo}^{+} e^{-j\vec{K}_{T00}\bullet\vec{\rho}} e^{-j\gamma_o z} \vec{u}_{moo} \tag{2.20}$$

$$\vec{H}_{inc} = \frac{1}{\sqrt{A}} \sum_{m=1}^{2} Y_{moo}^{o} A_{moo}^{+} e^{-j\vec{K}_{T00}\bullet\vec{\rho}} e^{-j\gamma_o z} (\vec{a}_z \times \vec{u}_{moo}) \tag{2.21}$$

On the other hand, the reflected fields in the same region are given by

$$\vec{E}_r = \frac{1}{\sqrt{A}} \sum_{m=1}^{2} A_{moo}^{-} e^{-j\vec{K}_{T00}\bullet\vec{\rho}} e^{+j\gamma_o z} \vec{u}_{moo} \tag{2.22}$$

$$\vec{H}_r = -\frac{1}{\sqrt{A}} \sum_{m=1}^{2} Y_{moo}^{o} A_{moo}^{-} e^{-j\vec{K}_{T00}\bullet\vec{\rho}} e^{+j\gamma_o z} (\vec{a}_z \times \vec{u}_{moo}) \tag{2.23}$$

where A_{moo}^{+} and A_{moo}^{-} is the magnitude of incident field component and the reflected field component, respectively. Furthermore, the subscripts m=1 and m=2 are used to designate TM and TE Floquet modes, respectively.

Then, the total transverse fields in the region left of dielectric ($z \le 0$), in the dielectric ($0 \le z \le t$) and in the region right of dielectric ($t \le z$) can be written as;

for $z \le 0$;

$$\vec{E}_o = \vec{E}_{inc} + \vec{E}_r = \frac{1}{\sqrt{A}} \sum_{m=1}^{2} [A_{moo}^{+} e^{-j\gamma_o z} + A_{moo}^{-} e^{+j\gamma_o z}] e^{-j\vec{K}_{T00}\bullet\vec{\rho}} \vec{u}_{moo} \tag{2.24}$$

$$\vec{H}_o = \vec{H}_{inc} + \vec{H}_r = \frac{1}{\sqrt{A}} \sum_{m=1}^{2} Y_{moo}^{o} [A_{moo}^{+} e^{-j\gamma_o z} - A_{moo}^{-} e^{+j\gamma_o z}] e^{-j\vec{K}_{T00}\bullet\vec{\rho}} (\vec{a}_z \times \vec{u}_{moo}) \tag{2.25}$$

for $0 \le z \le t$;

$$\vec{E}_1 = \frac{1}{\sqrt{A}} \sum_{m=1}^{2} [B_{moo}^{+} e^{-j\gamma_1 z} + B_{moo}^{-} e^{+j\gamma_1 z}] e^{-j\vec{K}_{T00}\bullet\vec{\rho}} \vec{u}_{moo} \tag{2.26}$$

$$\vec{H}_1 = \frac{1}{\sqrt{A}} \sum_{m=1}^{2} Y_{moo}^{1} [B_{moo}^{+} e^{-j\gamma_1 z} - B_{moo}^{-} e^{+j\gamma_1 z}] e^{-j\vec{K}_{T00}\bullet\vec{\rho}} (\vec{a}_z \times \vec{u}_{moo}) \tag{2.27}$$

and finally for $t \le z$;

$$\vec{E}_2 = \frac{1}{\sqrt{A}} \sum_{m=1}^{2} C_{moo}^{+} e^{-j\vec{K}_{T00}\bullet\vec{\rho}} e^{-j\gamma_o (z-t)} \vec{u}_{moo} \tag{2.28}$$

$$\vec{H}_2 = \frac{1}{\sqrt{A}} \sum_{m=1}^{2} Y_{moo}^{o} C_{moo}^{+} e^{-j\vec{K}_{T00}\bullet\vec{\rho}} e^{-j\gamma_o (z-t)} (\vec{a}_z \times \vec{u}_{moo}) \tag{2.29}$$

where the subscript and superscript 0 and 1 are used to determine the region that is air and dielectric, respectively. The superscripts + and – indicate the waves propagating along the positive z and negative z directions, respectively.

In order to find the unknown coefficients of the transverse fields, boundary conditions at z=0 and z=t should be applied to the tangential field components given in equations 2.24 to 2.29.

Then,

$$C^{+}_{moo} = \frac{4Y^{1}_{moo}Y^{o}_{moo}}{(Y^{1}_{moo}+Y^{o}_{moo})^{2}e^{j\gamma_1 t}-(Y^{1}_{moo}-Y^{o}_{moo})^{2}e^{-j\gamma_1 t}}A^{+}_{moo} \tag{2.30}$$

$$A^{-}_{moo} = \frac{[(Y^{o}_{moo})^{2}-(Y^{1}_{moo})^{2}]e^{j\gamma_1 t}+[(Y^{1}_{moo})^{2}-(Y^{o}_{moo})^{2}]e^{-j\gamma_1 t}}{(Y^{1}_{moo}+Y^{o}_{moo})^{2}e^{j\gamma_1 t}-(Y^{1}_{moo}-Y^{o}_{moo})^{2}e^{-j\gamma_1 t}}A^{+}_{moo} \tag{2.31}$$

where Y_{moo} is the modal admittance. In general, modal admittance is defined as,

$$Y^{i}_{mpq} = \begin{cases} \dfrac{Y_i k_i}{\gamma_i}, & \text{for TM modes} \quad (2.32) \\ \dfrac{Y_i \gamma_i}{k_i}, & \text{for TE modes} \quad (2.33) \end{cases}$$

where

$$i = \begin{cases} 0, & \text{for air} \\ 1, & \text{for dielectric} \end{cases} \qquad m = \begin{cases} 1, & \text{for TM mode} \\ 2, & \text{for TE mode} \end{cases}$$

$$Y_i = \sqrt{\frac{\varepsilon_i}{\mu_i}} \tag{2.34}$$

$$k_i = \omega\sqrt{\varepsilon_i \mu_i} \tag{2.35}$$

and

$$\gamma_i = \begin{cases} (k_i^{2} - \vec{K}_{Tpq} \bullet \vec{K}_{Tpq})^{1/2}, & \text{if } k_i^{2} > \left|\vec{K}_{Tpq}\right| \\ -j(\vec{K}_{Tpq} \bullet \vec{K}_{Tpq} - k_i^{2})^{1/2}, & \text{if } k_i^{2} < \left|\vec{K}_{Tpq}\right| \end{cases} \tag{2.36}$$

On the other hand as the incident wave illuminates the surface, currents are induced on the conducting elements. These induced currents on the metallic scatters then give rise to scattered fields which contain higher order Floquet modes which are necessary for the fulfillment of the boundary conditions. So, the scattered fields in the regions of interest are;

in the region $z\leq 0$;

$$\vec{E}_o^s = \frac{1}{\sqrt{A}} \sum_{m=1}^{2} \sum_{p=-\infty}^{\infty} \sum_{q=-\infty}^{\infty} A_{mpq}^{s-} e^{-j\vec{K}_{Tpq}\bullet\vec{\rho}} e^{+j\gamma_o z} \vec{u}_{mpq} \tag{2.37}$$

$$\vec{H}_o^s = -\frac{1}{\sqrt{A}} \sum_{m=1}^{2} \sum_{p=-\infty}^{\infty} \sum_{q=-\infty}^{\infty} Y_{mpq}^{o} A_{mpq}^{s-} e^{-j\vec{K}_{Tpq}\bullet\vec{\rho}} e^{+j\gamma_o z} (\vec{a}_z \times \vec{u}_{mpq}) \tag{2.38}$$

in the region $0\leq z\leq t$;

$$\vec{E}_1^s = \frac{1}{\sqrt{A}} \sum_{m=1}^{2} \sum_{p=-\infty}^{\infty} \sum_{q=-\infty}^{\infty} [B_{mpq}^{s+} e^{-j\gamma_1 z} + B_{mpq}^{s-} e^{+j\gamma_1 z}] e^{-j\vec{K}_{Tpq}\bullet\vec{\rho}} \vec{u}_{mpq} \tag{2.39}$$

$$\vec{H}_1^s = \frac{1}{\sqrt{A}} \sum_{m=1}^{2} \sum_{p=-\infty}^{\infty} \sum_{q=-\infty}^{\infty} Y_{mpq}^{1} [B_{mpq}^{s+} e^{-j\gamma_1 z} - B_{mpq}^{s-} e^{+j\gamma_1 z}] e^{-j\vec{K}_{Tpq}\bullet\vec{\rho}} (\vec{a}_z \times \vec{u}_{mpq}) \tag{2.40}$$

in the region $t\leq z$;

$$\vec{E}_2^s = \frac{1}{\sqrt{A}} \sum_{m=1}^{2} \sum_{p=-\infty}^{\infty} \sum_{q=-\infty}^{\infty} C_{mpq}^{s+} e^{-j\vec{K}_{Tpq}\bullet\vec{\rho}} e^{-j\gamma_o (z-t)} \vec{u}_{mpq} \tag{2.41}$$

$$\vec{H}_2^s = \frac{1}{\sqrt{A}} \sum_{m=1}^{2} \sum_{p=-\infty}^{\infty} \sum_{q=-\infty}^{\infty} Y_{mpq}^{o} C_{mpq}^{s+} e^{-j\vec{K}_{Tpq}\bullet\vec{\rho}} e^{-j\gamma_o (z-t)} (\vec{a}_z \times \vec{u}_{mpq}) \tag{2.42}$$

These fields must now satisfy the following boundary conditions:

I) The tangential components of the scattered electric fields must be continuous at z=0.

$$\vec{E}_o^s = \vec{E}_1^s$$

II) At z=0, the tangential component of the scattered magnetic fields are discontinuous by an amount equal to the induced current density on the metallic scatterers. That is,

$$\hat{n} \times [\vec{H}_1^s - \vec{H}_o^s] = \vec{J}_s$$

III) The tangential components of the scattered electric and magnetic fields are continuous at z=t.

$$\vec{E}_1^s = \vec{E}_2^s \quad \text{and} \quad \vec{H}_1^s = \vec{H}_2^s$$

Application of these boundary conditions when combined with the orthogonality property of the Floquet modes $\vec{\Psi}_{mpq}$ over a unit periodic cell enable us to express the coefficients of the scattered fields as;

$$A_{mpq}^{s-} = -\frac{1}{Y_{mpq}^{EQ}} \iint_S \vec{J}(x,y) \bullet \Psi_{mpq}^* dxdy \tag{2.43}$$

$$C_{mpq}^{s+} = \frac{2(Y_{mpq}^1)A_{mpq}^{s-}}{(Y_{mpq}^1 + Y_{mpq}^o)e^{+j\gamma_1 t} + (Y_{mpq}^1 - Y_{mpq}^o)e^{-j\gamma_1 t}} \tag{2.44}$$

where

$$\vec{J}(x,y) = \sum_{n=1}^{N} c_n \vec{I}_n(x,y) \tag{2.45}$$

$$Y_{mpq}^{EQ} = Y_{mpq}^o + Y_{mpq}^1 \left[\frac{(Y_{mpq}^1 + Y_{mpq}^o)e^{j\gamma_1 t} - (Y_{mpq}^1 - Y_{mpq}^o)e^{-j\gamma_1 t}}{(Y_{mpq}^1 + Y_{mpq}^o)e^{j\gamma_1 t} + (Y_{mpq}^1 - Y_{mpq}^o)e^{-j\gamma_1 t}} \right] \tag{2.46}$$

The asterisk designates the complex conjugate operation and c_n's are the unknown current density coefficients. Note that the unknown current density in (2.45) is expanded into a finite sum of terms having an assumed functional dependence but with unknown coefficients.

The total electric field in the region $z \le 0$, the reflected field and the transmitted field can then be written as,

$$\vec{E}_{tot} = \vec{E}_{inc} + \vec{E}_r + \vec{E}_o^s$$
$$= \frac{1}{\sqrt{A}}\left\{\sum_{m=1}^{2} A_{moo}^{+} e^{-j\vec{K}_{T00}\bullet\vec{\rho}} e^{-j\gamma_o z}\vec{u}_{moo} + \sum_{m=1}^{2} A_{moo}^{-} e^{-j\vec{K}_{T00}\bullet\vec{\rho}} e^{+j\gamma_o z}\vec{u}_{moo}\right.$$
$$\left. + \sum_{m=1}^{2}\sum_{p=-\infty}^{\infty}\sum_{q=-\infty}^{\infty} A_{mpq}^{s-} e^{-j\vec{K}_{Tpq}\bullet\vec{\rho}} e^{+j\gamma_o z}\vec{u}_{mpq}\right\} \quad (2.47)$$

$$\vec{E}_{ref} = \vec{E}_r + \vec{E}_o^s$$
$$= \frac{1}{\sqrt{A}}\left\{\sum_{m=1}^{2} A_{moo}^{-} e^{-j\vec{K}_{T00}\bullet\vec{\rho}} e^{+j\gamma_o z}\vec{u}_{moo} + \sum_{m=1}^{2}\sum_{p=-\infty}^{\infty}\sum_{q=-\infty}^{\infty} A_{mpq}^{s-} e^{-j\vec{K}_{Tpq}\bullet\vec{\rho}} e^{+j\gamma_o z}\vec{u}_{mpq}\right\} \quad (2.48)$$

$$\vec{E}_{trans} = \vec{E}_2 + \vec{E}_2^s$$
$$= \frac{1}{\sqrt{A}}\left\{\sum_{m=1}^{2} C_{moo}^{+} e^{-j\vec{K}_{T00}\bullet\vec{\rho}} e^{-j\gamma_o (z-t)}\vec{u}_{moo} + \sum_{m=1}^{2}\sum_{p=-\infty}^{\infty}\sum_{q=-\infty}^{\infty} C_{mpq}^{s+} e^{-j\vec{K}_{Tpq}\bullet\vec{\rho}} e^{-j\gamma_o (z-t)}\vec{u}_{mpq}\right\} \quad (2.49)$$

The coefficients in equations 2.47 - 2.49 are given in equations 2.30-31 and 2.43-44.

The only remaining boundary condition we have to satisfy is that the tangential component of the total electric field must vanish on the conducting elements:

$$\vec{E}_{tot} = 0 \qquad \text{at } z=0$$

That is,

$$\vec{E}_{tot} = 0 = \frac{1}{\sqrt{A}}\left\{\sum_{m=1}^{2} A_{moo}^{+} e^{-j\vec{K}_{T00}\bullet\vec{\rho}}\vec{u}_{moo} + \sum_{m=1}^{2} A_{moo}^{-} e^{-j\vec{K}_{T00}\bullet\vec{\rho}}\vec{u}_{moo}\right.$$
$$\left. + \sum_{m=1}^{2}\sum_{p=-\infty}^{\infty}\sum_{q=-\infty}^{\infty} \frac{1}{\sqrt{A}}\left(-\frac{1}{Y_{mpq}^{EQ}}\iint_S \vec{J}\bullet\vec{\Psi}_{mpq}^{*}\,dxdy\right) e^{-j\vec{K}_{Tpq}\bullet\vec{\rho}}\vec{u}_{mpq}\right\} \quad (2.50)$$

Substituting (2.19) and (2.45) into (2.50) yields,

$$-\left\{\sum_{m=1}^{2} A_{moo}^{+}\vec{\Psi}_{moo} + \sum_{m=1}^{2} A_{moo}^{-}\vec{\Psi}_{moo}\right\} = \sum_{m=1}^{2}\sum_{p=-\infty}^{\infty}\sum_{q=-\infty}^{\infty}\left(-\frac{1}{Y_{mpq}^{EQ}}\iint_S \vec{J}\bullet\vec{\Psi}_{mpq}^{*}\,dxdy\right)\vec{\Psi}_{mpq} \quad (2.51)$$

$$-\sum_{m=1}^{2}(A_{moo}^{+}+A_{moo}^{-})\vec{\Psi}_{moo}=\left[\sum_{m=1}^{2}\sum_{p=-\infty}^{\infty}\sum_{q=-\infty}^{\infty}(-\frac{1}{Y_{mpq}^{EQ}}\iint_{S}\vec{J}\bullet\vec{\Psi}_{mpq}^{*}dxdy)\vec{\Psi}_{mpq}\right] \tag{2.52}$$

Using the inner product defined by;

$$\langle f,g^{*}\rangle=\iint_{S}fg^{*}dxdy$$

we can write

$$\iint_{S}\vec{J}\bullet\vec{\Psi}_{mpq}^{*}dxdy=\sum_{n=1}^{N}c_{n}\langle\vec{I}_{n},\vec{\Psi}_{mpq}^{*}\rangle \tag{2.53}$$

and (2.52) then becomes

$$-\sum_{m=1}^{2}(A_{moo}^{+}+A_{moo}^{-})\vec{\Psi}_{moo}=\sum_{n=1}^{N}c_{n}\left[\sum_{m=1}^{2}\sum_{p=-\infty}^{\infty}\sum_{q=-\infty}^{\infty}(-\frac{1}{Y_{mpq}^{EQ}})\langle\vec{I}_{n},\vec{\Psi}_{mpq}^{*}\rangle\vec{\Psi}_{mpq}\right] \tag{2.54}$$

(2.54) is an integral equation in terms of the unknown current coefficients c_n. To solve this equation a set of N equations are obtained by taking the inner product of both sides of (2.54)with I_k, k=1,2,…,N. This process is the basis of the Moment Method discussed in the next chapter. This procedure yields the following set of equations:

$$-\sum_{m=1}^{2}(A_{moo}^{+}+A_{moo}^{-})\langle\vec{I}_{k},\vec{\Psi}_{moo}\rangle=\sum_{n=1}^{N}c_{n}\left[\sum_{m=1}^{2}\sum_{p=-\infty}^{\infty}\sum_{q=-\infty}^{\infty}(-\frac{1}{Y_{mpq}^{EQ}})\langle\vec{I}_{n},\vec{\Psi}_{mpq}^{*}\rangle\langle\vec{I}_{k},\vec{\Psi}_{mpq}\rangle\right]$$

$$k=1.\ 2.\ .\ .\ .\ ,N \tag{2.55}$$

(2.55) can be represented as a matrix equation

$$\begin{bmatrix}\mathbb{C}_{1}\\ \mathbb{C}_{2}\\ \vdots\\ \vdots\\ \mathbb{C}_{N}\end{bmatrix}=\begin{pmatrix}z_{11} & \cdots & z_{1N}\\ \vdots & \ddots & \vdots\\ z_{N1} & \cdots & z_{NN}\end{pmatrix}\begin{bmatrix}c_{1}\\ c_{2}\\ \vdots\\ \vdots\\ c_{N}\end{bmatrix} \tag{2.56}$$

where $\mathbb{C}_k$ is known as source vector, z_{ij} is impedance matrix and c_n is the current coefficients to be determined. That is,

$$\mathbb{C}_k = -\sum_{m=1}^{2} (A^{+}_{moo} + A^{-}_{moo}) \langle \vec{I}_k, \vec{\Psi}_{moo} \rangle \ , \qquad k=1,2,3\ldots..,N \qquad (2.57)$$

$$z_{ij} = -\frac{1}{Y^{EQ}_{mpq}} \sum_{mpq} \langle \vec{I}_i, \vec{\Psi}^{*}_{mpq} \rangle \langle \vec{\Psi}_{mpq}, \vec{I}_j \rangle \ , \qquad i,j = 1,2,....N \qquad (2.58)$$

where the triple summation $\sum_m \sum_p \sum_q$ is replaced by a single summation symbol $\sum_{mpq}$.

(2.56) can be solved using a matrix inversion algorithm. Once the unknown current coefficients are computed, scattered characteristics are obtained using (2.48) and (2.49).

CHAPTER 3

SOLUTION BY MOMENT METHOD

3.1 Determination of Basis Function

In Chapter 2, an integral equation is obtained for the current density induced on a conducting element in a single periodic unit cell, which is given by equation (2.52).

In order to solve equation (2.52) using Moment Method [17-19], current density should be approximated using an appropriate basis function. So, in the formulation piecewise triangular currents having unknown coefficients are adopted for the induced current density flowing on the conducting elements. The geometry of a triangular conducting element in a unit cell is shown in Figure 3.1.

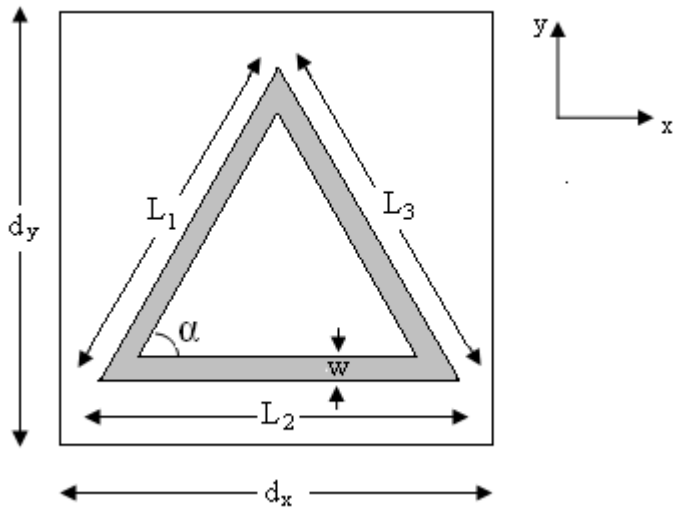

Figure 3.1 Geometry of triangular conducting element in a typical rectangular cell

The perimeter of the triangle is divided into segments and these segments are labeled as shown in Figure 3.2a

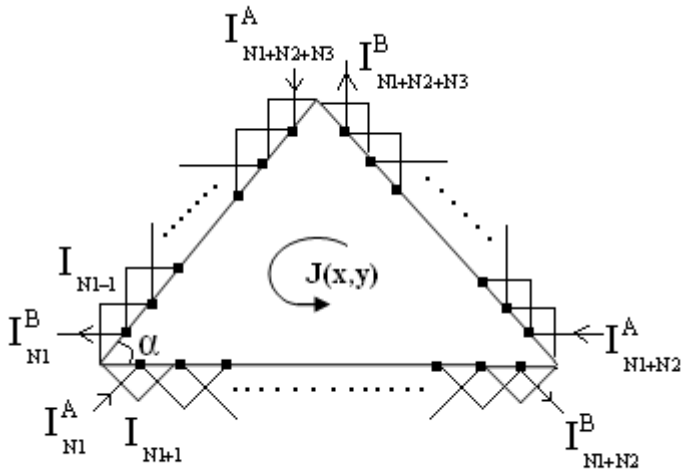

Figure 3.2a Piecewise triangular current distributions with unknown coefficients for triangular conducting element

Note that;

N_1=number of segments on 1st arm

N_2 =number of segments on horizontal arm

N_3 =number of segments on 3rd arm

So, total number of segments is $N_1+N_2+N_3$ and total number of currents is $N_1+N_2+N_3$.

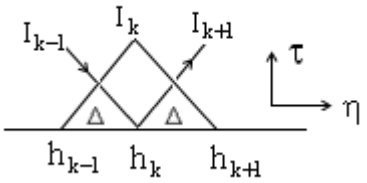

Figure 3.2b Approximated piecewise triangular current distribution

If the current on an arm is approximated by piecewise triangular currents as shown in Figure 3.2b, then for any current $J_{n,k}$ flowing from h_{k-1} to h_{k+1} along the η-axis we can write;

$$J_{n,k}(\eta,\tau)=\begin{cases}\dfrac{I_k}{\Delta_n}(\eta-h_{k-1}) & h_{k-1}\le\eta\le h_k\\ \dfrac{I_k}{\Delta_n}(h_{k+1}-\eta) & h_k\le\eta\le h_{k+1}\end{cases} \tag{3.1}$$

Note that $h_k = h_{k-1} + \Delta_n$ and $h_{k+1} = h_k + \Delta_n$ where Δ_n is the segment size. Subscripts n (1, 2, or 3) indicates the n^{th} arm of the triangle and k indicates the segment number which supports the current I_k.

3.2 Calculation of Inner Products

General form of the inner products for the impedance matrix is given in equation (2.53) in previous chapter. When this equation is written explicitly, the inner products that we have to compute in this case are of the form

$$\langle \vec{J}(x,y), \vec{\Psi}^*_{mpq}(x,y) \rangle = \iint_{\text{unit cell}} e^{j(xk_{xpq} + yk_{ypq})} \begin{bmatrix} \vec{u}^{TM}_{pq} \\ \vec{u}^{TE}_{pq} \end{bmatrix} \bullet \vec{J}(x,y)dxdy \tag{3.2}$$

Since there are three arms, it will be easier to formula the problem considering the current in each arm separately.

3.2.1 First slant arm

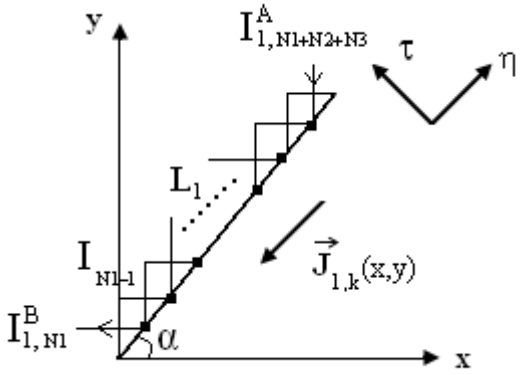

Figure 3.3 Piecewise current distribution on the first slant arm

Let us assume that this side is divided into N_1 segments where the $N_1{}^{th}$ point is a corner point of the triangle and let the segment size of the first slant arm is Δ_1.

However, in the following formulation the subscript 1 will be dropped and Δ will be used for Δ_1. Furthermore, note that the current $\vec{J}_{1k}(x,y)$ actually flows in $(-\vec{a}_\eta)$ direction on this arm where

$$\vec{a}_\eta = \vec{a}_x \cos\alpha + \vec{a}_y \sin\alpha$$

So using equation 3.2, the inner product for the current $\vec{J}_{1,k}(x,y)$ flowing in this arm can be written as

$$\langle \vec{J}_{1,k}(x,y), \vec{\Psi}^*_{mpq}(x,y) \rangle = -\vec{a}_\eta \bullet \begin{bmatrix} \vec{u}^{TM}_{pq} \\ \vec{u}^{TE}_{pq} \end{bmatrix} \iint_{\text{unit cell}} e^{j(xk_{xpq} + yk_{ypq})} J_{1,k}(x,y)\,dxdy \tag{3.3}$$

Since this arm runs along η-axis, (3.3) can be evaluated easily by changing the variables from (x,y) to (η,τ). This is achieved by using the transformation;

$$\begin{aligned} x &= \eta\cos\alpha - \tau\sin\alpha \\ y &= \eta\sin\alpha + \tau\cos\alpha \end{aligned} \tag{3.4}$$

Then substituting (3.4) into (3.3) yields

$$\langle \vec{J}_{1,k}(x,y), \vec{\Psi}^*_{mpq}(x,y) \rangle = -\vec{a}_\eta \bullet \begin{bmatrix} \vec{u}^{TM}_{pq} \\ \vec{u}^{TE}_{pq} \end{bmatrix} \iint_{\text{unit cell}} e^{j(\eta\cos\alpha - \tau\sin\alpha)k_{xpq}} e^{j(\eta\sin\alpha + \tau\cos\alpha)k_{ypq}} J_{1,k}(\eta,\tau)\,d\eta d\tau \tag{3.5}$$

Now let

$$\begin{aligned} s_{pq} &= k_{xpq}\cos\alpha + k_{ypq}\sin\alpha \\ t_{pq} &= -k_{xpq}\sin\alpha + k_{ypq}\cos\alpha \end{aligned}$$

Using these parameters in (3.5) gives

$$\langle \vec{J}_{1,k}, \vec{\Psi}^*_{mpq} \rangle = -\vec{a}_\eta \bullet \begin{bmatrix} \vec{u}^{TM}_{pq} \\ \vec{u}^{TE}_{pq} \end{bmatrix} \iint_{\text{unit cell}} e^{j\eta s_{pq}} e^{j\tau t_{pq}} J_{1,k}(\eta,\tau)\,d\eta d\tau \tag{3.6}$$

Substitution of (3.1) into (3.6) yields a typical inner product for the current on the first slant arm of the form

$$\langle \vec{I}_{l,k}, \vec{\Psi}^{*}_{mpq} \rangle = -\vec{a}_{\eta} \bullet \begin{bmatrix} \vec{u}^{TM}_{pq} \\ \vec{u}^{TE}_{pq} \end{bmatrix} \int_{-w/2}^{w/2} e^{j\tau t_{pq}} d\tau \left\{ \frac{1}{\Delta} \int_{h_{k-1}}^{h_k} e^{j\eta s_{pq}} (\eta - h_{k-1}) d\eta + \frac{1}{\Delta} \int_{h_k}^{h_{k+1}} e^{j\eta s_{pq}} (h_{k+1} - \eta) d\eta \right\} \tag{3.7}$$

On the other hand, inner products for the corner points are given by

I) for the last point (k=last=N_1+N_2+N_3)

$$\langle \vec{I}^{A}_{l,last}, \vec{\Psi}^{*}_{mpq} \rangle = -\vec{a}_{\eta} \bullet \begin{bmatrix} \vec{u}^{TM}_{pq} \\ \vec{u}^{TE}_{pq} \end{bmatrix} \int_{-w/2}^{w/2} e^{j\tau t_{pq}} d\tau \left\{ \frac{1}{\Delta} \int_{L_1-\Delta}^{L_1} e^{j\eta s_{pq}} \left[\eta - (L_1 - \Delta) \right] d\eta \right\} \tag{3.8}$$

and

II) for the $N_1{}^{th}$ point (k=N_1)

$$\langle \vec{I}^{B}_{l,N_1}, \vec{\Psi}^{*}_{mpq} \rangle = -\vec{a}_{\eta} \bullet \begin{bmatrix} \vec{u}^{TM}_{pq} \\ \vec{u}^{TE}_{pq} \end{bmatrix} \int_{-w/2}^{w/2} e^{j\tau t_{pq}} d\tau \left\{ \frac{1}{\Delta} \int_{0}^{\Delta} e^{j\eta s_{pq}} \left[\Delta - \eta) \right] d\eta \right\} \tag{3.9}$$

Evaluation of integrals in (3.7), (3.8) and (3.9) yield

$$\langle \vec{I}_{l,k}, \vec{\Psi}^{*}_{mpq} \rangle = -\vec{a}_{\eta} \bullet \begin{bmatrix} \vec{u}^{TM}_{pq} \\ \vec{u}^{TE}_{pq} \end{bmatrix} \left[\frac{w \sin(w/2\, t_{pq})}{(w/2\, t_{pq})} \right] \left[\frac{1}{s^2_{pq} \Delta} (-e^{j s_{pq} h_{k-1}} + 2e^{j s_{pq} h_k} - e^{j s_{pq} h_{k+1}}) \right], s_{pq} \neq 0 \tag{3.10a}$$

$$\langle \vec{I}_{l,k}, \vec{\Psi}^{*}_{mpq} \rangle = -\vec{a}_{\eta} \bullet \begin{bmatrix} \vec{u}^{TM}_{pq} \\ \vec{u}^{TE}_{pq} \end{bmatrix} \left[\frac{w \sin(w/2\, t_{pq})}{(w/2\, t_{pq})} \right] (\Delta), \quad s_{pq} = 0 \tag{3.10b}$$

$$\langle \vec{I}^{A}_{l,last}, \vec{\Psi}^{*}_{mpq} \rangle = -\vec{a}_{\eta} \bullet \begin{bmatrix} \vec{u}^{TM}_{pq} \\ \vec{u}^{TE}_{pq} \end{bmatrix} \left[\frac{w \sin(w/2\, t_{pq})}{(w/2\, t_{pq})} \right] \left[\frac{1}{s^2_{pq} \Delta} (e^{j L_1 s_{pq}} (1 - j s_{pq} \Delta) - e^{j(L_1 - \Delta) s_{pq}}) \right], s_{pq} \neq 0 \tag{3.11a}$$

$$\langle \vec{I}^{A}_{l,last}, \vec{\Psi}^{*}_{mpq} \rangle = -\vec{a}_{\eta} \bullet \begin{bmatrix} \vec{u}^{TM}_{pq} \\ \vec{u}^{TE}_{pq} \end{bmatrix} \left[\frac{w \sin(w/2\, t_{pq})}{(w/2\, t_{pq})} \right] (\Delta/2), \quad s_{pq} = 0 \tag{3.11b}$$

$$\langle \vec{I}^{B}_{1,N_1}, \vec{\Psi}^{*}_{mpq} \rangle = -\vec{a}_\eta \bullet \begin{bmatrix} \vec{u}^{TM}_{pq} \\ \vec{u}^{TE}_{pq} \end{bmatrix} \left[\frac{w \sin(w/2\, t_{pq})}{(w/2\, t_{pq})} \right] \left[\frac{1}{s^2_{pq}\Delta} \left[(1 + j s_{pq}\Delta) - e^{j s_{pq}\Delta} \right] \right], \quad s_{pq} \neq 0 \tag{3.12a}$$

$$\langle \vec{I}^{B}_{1,N_1}, \vec{\Psi}^{*}_{mpq} \rangle = -\vec{a}_\eta \bullet \begin{bmatrix} \vec{u}^{TM}_{pq} \\ \vec{u}^{TE}_{pq} \end{bmatrix} \left[\frac{w \sin(w/2\, t_{pq})}{(w/2\, t_{pq})} \right] (\Delta/2), \quad s_{pq} = 0 \tag{3.12b}$$

3.2.2 Horizontal arm

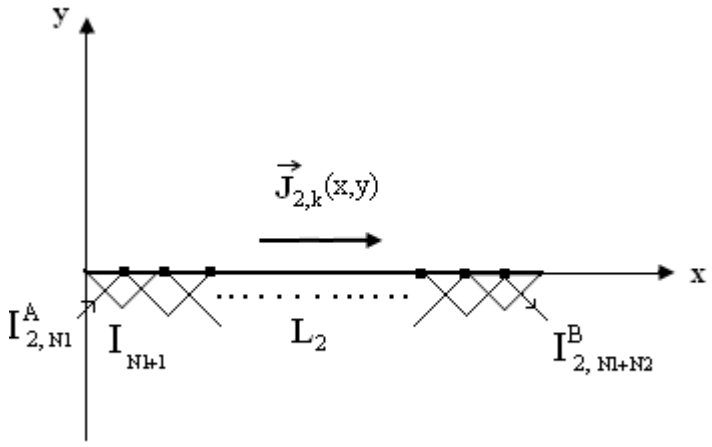

Figure 3.4 Piecewise current distribution on the horizontal arm

Let us assume that the horizontal arm is divided into N_2 segments. The horizontal arm starts at point N_1 and ends at point N_1+N_2 which are the corner points for the horizontal arm. On the other hand, the segment size Δ_2 of the horizontal arm may not necessarily be equal to the segment size Δ_1 of the first arm. In the formulation of inner products, the subscript of the segment size is dropped and Δ is also used instead of Δ_2 for simplicity. Furthermore, the current $\vec{J}_{2,k}(x,y)$ flows in $(+\vec{a}_x)$ direction on this arm. For this reason, along the horizontal arm the inner products take the form

$$\langle \vec{J}_{2,k}(x,y), \vec{\Psi}^{*}_{mpq}(x,y) \rangle = \vec{a}_x \bullet \begin{bmatrix} \vec{u}^{TM}_{pq} \\ \vec{u}^{TE}_{pq} \end{bmatrix} \iint_{\text{unit cell}} e^{j(xk_{xpq} + yk_{ypq})} J_{2,k}(x,y)\,dx\,dy \tag{3.13}$$

When the current $\vec{J}_{2,k}(x,y)$ is expanded in terms of piecewise triangular functions then a typical inner product for this arm is of the form

$$\langle \vec{I}_{2,k}, \vec{\Psi}^{*}_{mpq} \rangle = \vec{a}_x \bullet \begin{bmatrix} \vec{u}^{TM}_{pq} \\ \vec{u}^{TE}_{pq} \end{bmatrix} \int_{-w/2}^{w/2} e^{jyk_{ypq}} dy \left\{ \frac{1}{\Delta} \int_{h_{k-1}}^{h_k} e^{jxk_{xpq}} (x - h_{k-1}) dx + \frac{1}{\Delta} \int_{h_k}^{h_{k+1}} e^{jxk_{xpq}} (h_{k+1} - x) dx \right\} \tag{3.14}$$

On the other hand, inner products for the corner points are given by

I) for the N_1^{th} point ($k=N_1$)

$$\langle \vec{I}^{A}_{2,N_1}, \vec{\Psi}^{*}_{mpq} \rangle = \vec{a}_x \bullet \begin{bmatrix} \vec{u}^{TM}_{pq} \\ \vec{u}^{TE}_{pq} \end{bmatrix} \int_{-w/2}^{w/2} e^{jyk_{ypq}} dy \left[\frac{1}{\Delta} \int_{0}^{\Delta} e^{jxk_{xpq}} (\Delta - x) dx \right] \tag{3.15}$$

and

II) for the $(N_1+N_2)^{th}$ point ($k=N_1+N_2$)

$$\langle \vec{I}^{B}_{2,N_1+N_2}, \vec{\Psi}^{*}_{mpq} \rangle = \vec{a}_x \bullet \begin{bmatrix} \vec{u}^{TM}_{pq} \\ \vec{u}^{TE}_{pq} \end{bmatrix} \int_{-w/2}^{w/2} e^{jyk_{ypq}} dy \left[\frac{1}{\Delta} \int_{L_2-\Delta}^{L_2} e^{jxk_{xpq}} (x - (L_2 - \Delta)) dx \right] \tag{3.16}$$

When we evaluate the integrals in the equations, inner products for the horizontal arm and the corners at points N_1^{th} and $(N_1+N_2)^{th}$ have the following forms.

$$\langle \vec{I}_{2,k}, \vec{\Psi}^{*}_{mpq} \rangle = \vec{a}_x \bullet \begin{bmatrix} \vec{u}^{TM}_{pq} \\ \vec{u}^{TE}_{pq} \end{bmatrix} \left[\frac{w \sin(w/2\, k_{ypq})}{(w/2\, k_{ypq})} \right] \left[\frac{1}{k^2_{xpq}\Delta} (-e^{jk_{xpq}h_{k-1}} + 2e^{jk_{xpq}h_k} - e^{jk_{xpq}h_{k+1}}) \right], \; k_{xpq} \neq 0 \tag{3.17a}$$

$$\langle \vec{I}_{2,k}, \vec{\Psi}^{*}_{mpq} \rangle = \vec{a}_x \bullet \begin{bmatrix} \vec{u}^{TM}_{pq} \\ \vec{u}^{TE}_{pq} \end{bmatrix} \left[\frac{w \sin(w/2\, k_{ypq})}{(w/2\, k_{ypq})} \right] (\Delta) \;, k_{xpq} = 0 \tag{3.17b}$$

$$\langle \vec{I}^{A}_{2,N_1}, \vec{\Psi}^{*}_{mpq} \rangle = \vec{a}_x \bullet \begin{bmatrix} \vec{u}^{TM}_{pq} \\ \vec{u}^{TE}_{pq} \end{bmatrix} \left[\frac{w \sin(w/2\, k_{ypq})}{(w/2\, k_{ypq})} \right] \left[\frac{1}{k^2_{xpq}\Delta} \left[(1 + jk_{xpq}\Delta) - e^{jk_{xpq}\Delta} \right] \right], k_{xpq} \neq 0 \tag{3.18a}$$

$$\langle \vec{I}^{A}_{2,N_1}, \vec{\Psi}^{*}_{mpq} \rangle = \vec{a}_x \bullet \begin{bmatrix} \vec{u}^{TM}_{pq} \\ \vec{u}^{TE}_{pq} \end{bmatrix} \left[\frac{w \sin(w/2\, k_{ypq})}{(w/2\, k_{ypq})} \right] \Delta/2, \;\; k_{xpq} = 0 \tag{3.18b}$$

$$\langle \vec{I}^{B}_{2,N_1+N_2}, \vec{\Psi}^{*}_{mpq} \rangle = \vec{a}_x \bullet \begin{bmatrix} \vec{u}^{TM}_{pq} \\ \vec{u}^{TE}_{pq} \end{bmatrix} \left[\frac{w \sin(w/2\, k_{ypq})}{(w/2\, k_{ypq})} \right] \left[\frac{1}{k^2_{xpq}\Delta} \left[e^{jk_{xpq}L_2}(1 - jk_{xpq}\Delta) - e^{jk_{xpq}(L_2-\Delta)} \right] \right], \; k_{xpq} \neq 0 \tag{3.19a}$$

$$\langle \vec{I}^{B}_{2,N_1+N_2}, \vec{\Psi}^{*}_{mpq} \rangle = \vec{a}_x \bullet \begin{bmatrix} \vec{u}^{TM}_{pq} \\ \vec{u}^{TE}_{pq} \end{bmatrix} \left[\frac{w \sin(w/2\, k_{ypq})}{(w/2\, k_{ypq})} \right] \Delta/2, \quad k_{xpq} = 0 \tag{3.19b}$$

3.2.3 Third arm

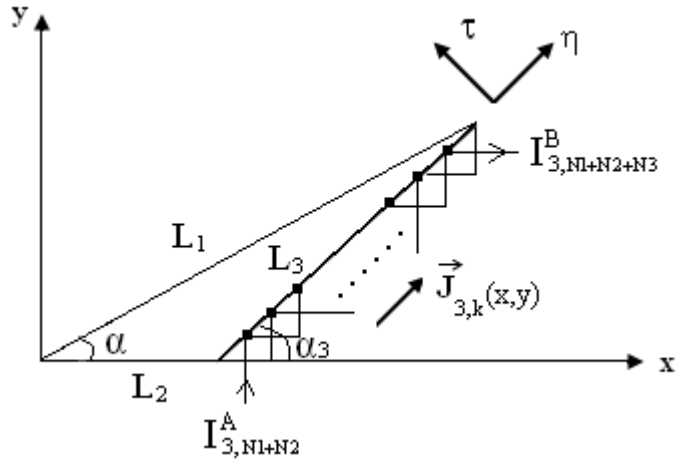

Figure 3.5 Piecewise current distribution on the third arm

From the Figure 3.5 it is seen that the third side makes an angle α_3 with respect to the x-axis and the current $\vec{J}_{3,k}(x, y)$ flows in $(\vec{a}_\eta)$ direction on this arm where

$\vec{a}_\eta = \vec{a}_x \cos\alpha + \vec{a}_y \sin\alpha$ (subscript 3 is dropped)

The transformation in this case requires, in addition to the rotation of the axis, a translation. That is, transformation from (x, y) to (η, τ) needs the following change of variables.

$$\begin{aligned} x &= L_2 + \eta\cos\alpha - \tau\sin\alpha \\ y &= \eta\sin\alpha + \tau\cos\alpha \end{aligned} \tag{3.20}$$

Making use of 3.2, the inner product of the Floquet modes with the current $\vec{J}_{3,k}(x, y)$ flowing in the third arm can be written as

$$\langle \vec{J}_{3,k}(x,y), \vec{\Psi}^{*}_{mpq}(x,y)\rangle = \vec{a}_{\eta} \bullet \begin{bmatrix} \vec{u}^{TM}_{pq} \\ \vec{u}^{TE}_{pq} \end{bmatrix} \iint_{\text{unit cell}} e^{j(xk_{xpq}+yk_{ypq})} J_{3,k}(x,y)dxdy \tag{3.21}$$

Using the transformation (3.20) in (3.21) yields

$$\langle \vec{J}_{3,k}(x,y), \vec{\Psi}^{*}_{mpq}(x,y)\rangle = \vec{a}_{\eta} \bullet \begin{bmatrix} \vec{u}^{TM}_{pq} \\ \vec{u}^{TE}_{pq} \end{bmatrix} e^{-jk_{xpq}L_2} \iint_{\text{unit cell}} e^{j\eta(k_{xpq}\cos\alpha + k_{ypq}\sin\alpha)} e^{j\tau(-k_{xpq}\sin\alpha + k_{ypq}\cos\alpha)} J_{3,k}(\eta,\tau)d\eta d\tau \tag{3.22}$$

Now if we let
$$\begin{aligned} s_{pq} &= k_{xpq}\cos\alpha + k_{ypq}\sin\alpha \\ t_{pq} &= -k_{xpq}\sin\alpha + k_{ypq}\cos\alpha \end{aligned}$$

(3.22) becomes

$$\langle \vec{J}_{3,k}, \vec{\Psi}^{*}_{mpq}\rangle = \vec{a}_{\eta} \bullet \begin{bmatrix} \vec{u}^{TM}_{pq} \\ \vec{u}^{TE}_{pq} \end{bmatrix} e^{k_{xpq}L_2} \iint_{\text{unit cell}} e^{j\eta s_{pq}} e^{j\tau t_{pq}} J_{3,k}(\eta,\tau)d\eta d\tau \tag{3.23}$$

When the current $J_{3,k}(\eta,\tau)$ is expressed in terms of piecewise triangular functions, a typical inner product in this case will be of the form;

$$\langle \vec{I}_{3,k}, \vec{\Psi}^{*}_{mpq}\rangle = \vec{a}_{\eta} \bullet \begin{bmatrix} \vec{u}^{TM}_{pq} \\ \vec{u}^{TE}_{pq} \end{bmatrix} e^{jk_{xpq}L_2} \int_{-w/2}^{w/2} e^{j\tau t_{pq}} d\tau \left\{ \frac{1}{\Delta} \int_{h_{k-1}}^{h_k} e^{j\eta s_{pq}} (\eta - h_{k-1})d\eta + \frac{1}{\Delta} \int_{h_k}^{h_{k+1}} e^{j\eta s_{pq}} (h_{k+1} - \eta)d\eta \right\} \tag{3.24}$$

and the inner products for the corner points are given by

I) for the $(N_1+N_2)^{th}$ point ($k=N_1+N_2$)

$$\langle \vec{I}^{A}_{3,N_1+N_2}, \vec{\Psi}^{*}_{mpq}\rangle = \vec{a}_{\eta} \bullet \begin{bmatrix} \vec{u}^{TM}_{pq} \\ \vec{u}^{TE}_{pq} \end{bmatrix} \int_{-w/2}^{w/2} e^{j\tau t_{pq}} d\tau \left\{ \frac{e^{jk_{xpq}L_2}}{\Delta} \int_{0}^{\Delta} e^{j\eta s_{pq}} (\Delta - \eta)d\eta \right\} \tag{3.25}$$

II) for the last point ($k=last=N_1+N_2+N_3$)

$$\langle \vec{I}^{B}_{3,last}, \vec{\Psi}^{*}_{mpq}\rangle = \vec{a}_{\eta} \bullet \begin{bmatrix} \vec{u}^{TM}_{pq} \\ \vec{u}^{TE}_{pq} \end{bmatrix} \int_{-w/2}^{w/2} e^{j\tau t_{pq}} d\tau \left\{ \frac{e^{jk_{xpq}L_2}}{\Delta} \int_{L_3-\Delta}^{L_3} e^{j\eta s_{pq}} \left[\eta - (L_3 - \Delta)\right] d\eta \right\} \tag{3.26}$$

When the above integrals are evaluated we obtain the following expressions.

$$\langle \vec{I}_{3,k}, \vec{\Psi}^{*}_{mpq} \rangle = \vec{a}_{\eta} \bullet \begin{bmatrix} \vec{u}^{TM}_{pq} \\ \vec{u}^{TE}_{pq} \end{bmatrix} \left[\frac{w \sin(w/2\, t_{pq})}{(w/2\, t_{pq})} \right] \left[\frac{e^{jk_{xpq}L_2}}{s^2_{pq}\Delta} (-e^{js_{pq}h_{k-1}} + 2e^{js_{pq}h_k} - e^{js_{pq}h_{k+1}}) \right] \;,\; s_{pq} \neq 0 \tag{3.27a}$$

$$\langle \vec{I}_{3,k}, \vec{\Psi}^{*}_{mpq} \rangle = \vec{a}_{\eta} \bullet \begin{bmatrix} \vec{u}^{TM}_{pq} \\ \vec{u}^{TE}_{pq} \end{bmatrix} \left[\frac{w \sin(w/2\, t_{pq})}{(w/2\, t_{pq})} \right] e^{jk_{xpq}L_2} (\Delta) \;,\; s_{pq} = 0 \tag{3.27b}$$

$$\langle \vec{I}^{A}_{3,N_1+N_2}, \vec{\Psi}^{*}_{mpq} \rangle = \vec{a}_{\eta} \bullet \begin{bmatrix} \vec{u}^{TM}_{pq} \\ \vec{u}^{TE}_{pq} \end{bmatrix} \left[\frac{w \sin(w/2\, t_{pq})}{(w/2\, t_{pq})} \right] \left[\frac{e^{jk_{xpq}L_2}}{s^2_{pq}\Delta} \left[(1 + js_{pq}\Delta) - e^{js_{pq}\Delta} \right] \right], \; s_{pq} \neq 0 \tag{3.28a}$$

$$\langle \vec{I}^{A}_{3,N_1+N_2}, \vec{\Psi}^{*}_{mpq} \rangle = \vec{a}_{\eta} \bullet \begin{bmatrix} \vec{u}^{TM}_{pq} \\ \vec{u}^{TE}_{pq} \end{bmatrix} \left[\frac{w \sin(w/2\, t_{pq})}{(w/2\, t_{pq})} \right] e^{jk_{xpq}L_2} (\Delta/2) \qquad s_{pq} = 0 \tag{3.28b}$$

$$\langle \vec{I}^{B}_{3,last}, \vec{\Psi}^{*}_{mpq} \rangle = \vec{a}_{\eta} \bullet \begin{bmatrix} \vec{u}^{TM}_{pq} \\ \vec{u}^{TE}_{pq} \end{bmatrix} \left[\frac{w \sin(w/2\, t_{pq})}{(w/2\, t_{pq})} \right] \left[\frac{e^{jk_{xpq}L_2}}{s^2_{pq}\Delta} \right] \left[e^{js_{pq}L_3} (1 - js_{pq}\Delta) - e^{j(L_3 - \Delta)s_{pq}} \right], \; s_{pq} \neq 0 \tag{3.29a}$$

$$\langle \vec{I}^{B}_{3,last}, \vec{\Psi}^{*}_{mpq} \rangle = \vec{a}_{\eta} \bullet \begin{bmatrix} \vec{u}^{TM}_{pq} \\ \vec{u}^{TE}_{pq} \end{bmatrix} \left[\frac{w \sin(w/2\, t_{pq})}{(w/2\, t_{pq})} \right] e^{jk_{xpq}L_2} (\Delta/2), \qquad s_{pq} = 0 \tag{3.29b}$$

Choosing proper p, q values and using the above inner products, equation (2.55) can be written in the matrix form as follows

$$\begin{bmatrix} \mathbb{C}_1 \\ \mathbb{C}_2 \\ \vdots \\ \vdots \\ \mathbb{C}_N \end{bmatrix} = \begin{pmatrix} z_{11} & \cdots & z_{1N} \\ \vdots & \ddots & \vdots \\ z_{N1} & \cdots & z_{NN} \end{pmatrix} \begin{bmatrix} c_1 \\ c_2 \\ \vdots \\ \vdots \\ c_N \end{bmatrix} \tag{3.30}$$

where $\mathbb{C}_k$ is known as source vector, z_{ij} is impedance matrix and c_n is the current coefficients to be found. Then,

$$\mathbb{C}_k = -\sum_{m=1}^{2} (A^{+}_{moo} + A^{-}_{moo}) \langle \vec{I}_k, \vec{\Psi}_{moo} \rangle \ , \qquad k=1,2,3\ldots..,N \qquad (3.31)$$

$$z_{ij} = -\frac{1}{Y^{EQ}_{mpq}} \sum_{mpq} \langle \vec{I}_i, \vec{\Psi}^{*}_{mpq} \rangle \langle \vec{\Psi}_{mpq}, \vec{I}_j \rangle \ , \qquad i,j = 1,2,....N \qquad (3.32)$$

where the triple summation $\sum_m \sum_p \sum_q$ is replaced by a single summation symbol $\sum_{mpq}$.

Once the impedance matrix and the source vector i.e. $\mathbb{C}_k$'s are calculated then the unknown current coefficients $c_1, c_2, c_3, ..., c_N$ can be determined by taking the inverse of the matrix given in 3.30. Then, the reflected and transmitted fields can be calculated using these current coefficients.

3.3 Comparison with Previous Works

Since there is no study related to FSSs comprising of triangular conducting elements in literature, our results are compared with the experimental and the theoretical results given in the literature for FSSs formed using conducting strips and L-shaped conductors. Due to the flexibility of the algorithm we developed for the FSSs having triangular conducting elements, FSSs comprising of conducting strips and L dipoles can be analyzed simply by removing the appropriate arms of the triangles.

3.3.1 FSSs with conducting strips

As can be seen from Figure 3.1, when the arms L_2 and L_3 of the triangle are taken as zero (L_2=L_3=0) and the angle α is set equal to 90°, an FSS with vertical strips is obtained.

To compare our results with the results for a FSS comprising of free standing strips quoted in [4] our program is used to compute the power reflection coefficient by

choosing L_2=L_3=0 and α =90 and using the parameter set given in Figure 3.6. In the analysis 10 piecewise triangular basis functions are used.

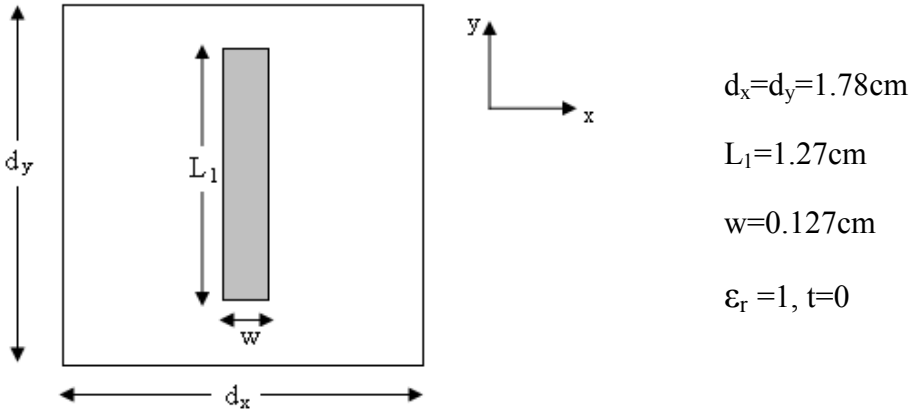

Figure 3.6 Geometry of the unit cell of the frequency selective surfaces composed of strips

As seen in Figure 3.7, our results are almost exact with the values measured by Ott, Kouyoumjian and Peters [4]. The graph shows a total reflection at 11.1GHz for a freestanding FSS structure comprising of conducting strips when the structure is illuminated by a normally incident plane wave..

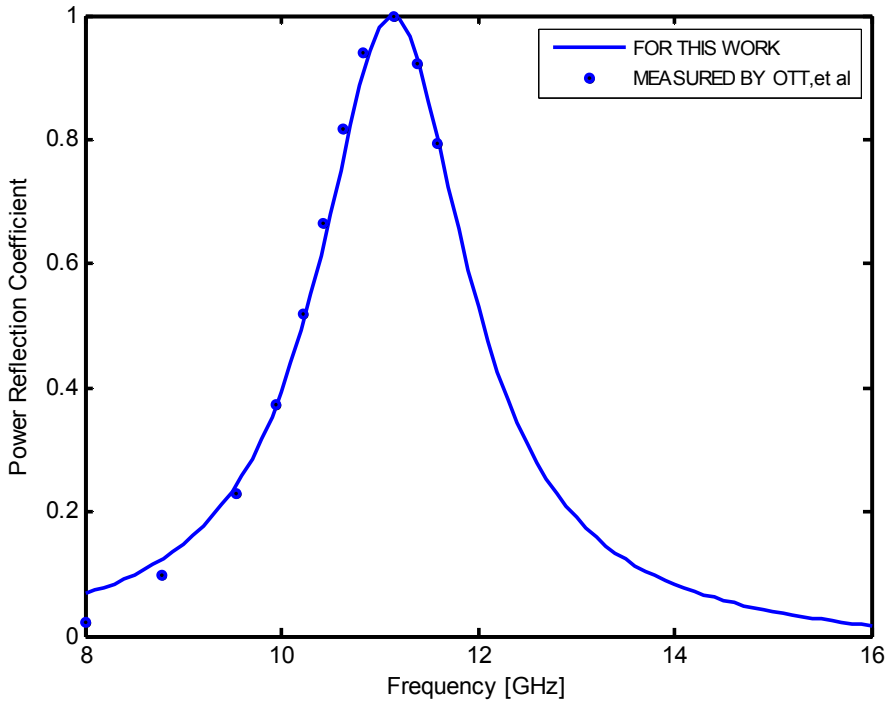

Figure 3.7 TE Power reflection coefficient versus frequency for the freestanding strip FSS

At the resonant frequency magnitude of the current is equal to its real part. For this reason, distribution of induced currents on a conducting element is also plotted at the resonant frequency. Figure 3.8 shows the normalized current versus length of the narrow strip at 11.1GHz.

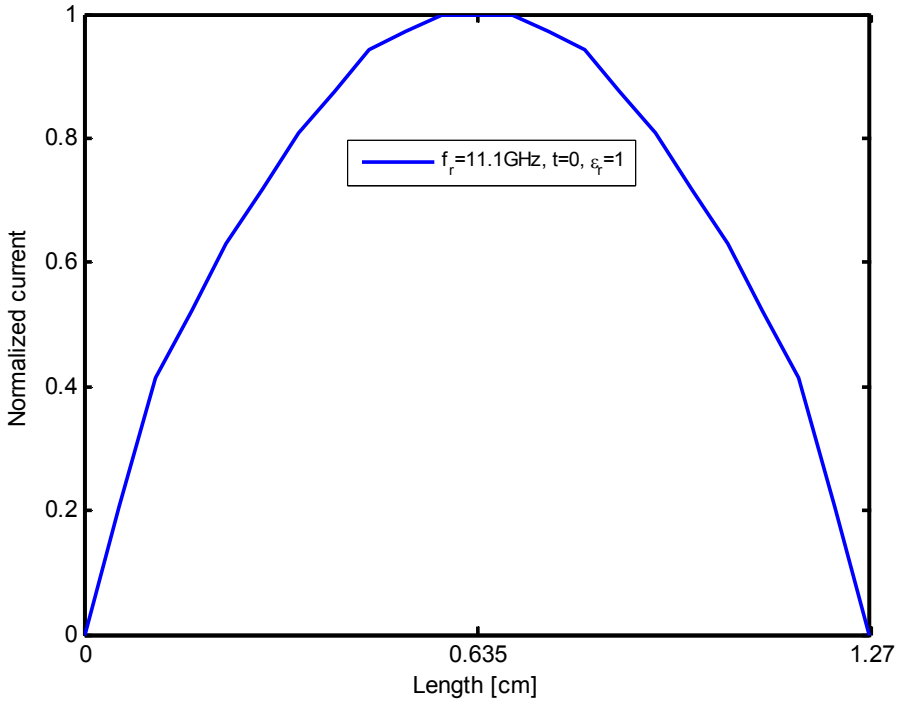

Figure 3.8 Normalized current versus length for the freestanding strip FSS at resonance frequency of TE incidence

3.3.2 FSSs with L-dipoles

Our algorithm for the case of triangular shaped conducting elements can also be used to obtain scattering characteristics of FSSs comprising of L-shaped dipoles simply by choosing the length of the third arm of the triangle equal to zero (L_3=0) and the angle α to 90°. The geometry of a unit cell with an L-shaped conductor is shown in Figure 3.9 we can also obtain scattering characteristics of FSSs comprising of V-shaped elements using our software.

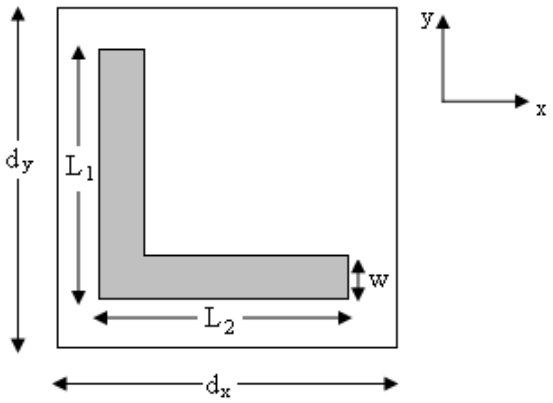

Figure 3.9 Frequency Selective Surface with L-shape conductor

Extensive work has been done on FSSs comprising of L-shaped dipoles by Delihacıoğlu [14]. However, when our program is used to compare our results for L-shaped dipoles with his results major discrepancies are found. For example, for L_1= L_2=0.9cm, w=0.09cm, d_x=d_y=0.93cm, t=0.1cm, ε_r =1.6, N=19, and p=q=9 Delihacıoğlu shows the existence of a total reflection at 13.4 GHz for a normally incident plane wave as can be seen in Figure 3.10a whereas our results presented in Figure 3.10b show that such a resonance does not occur.

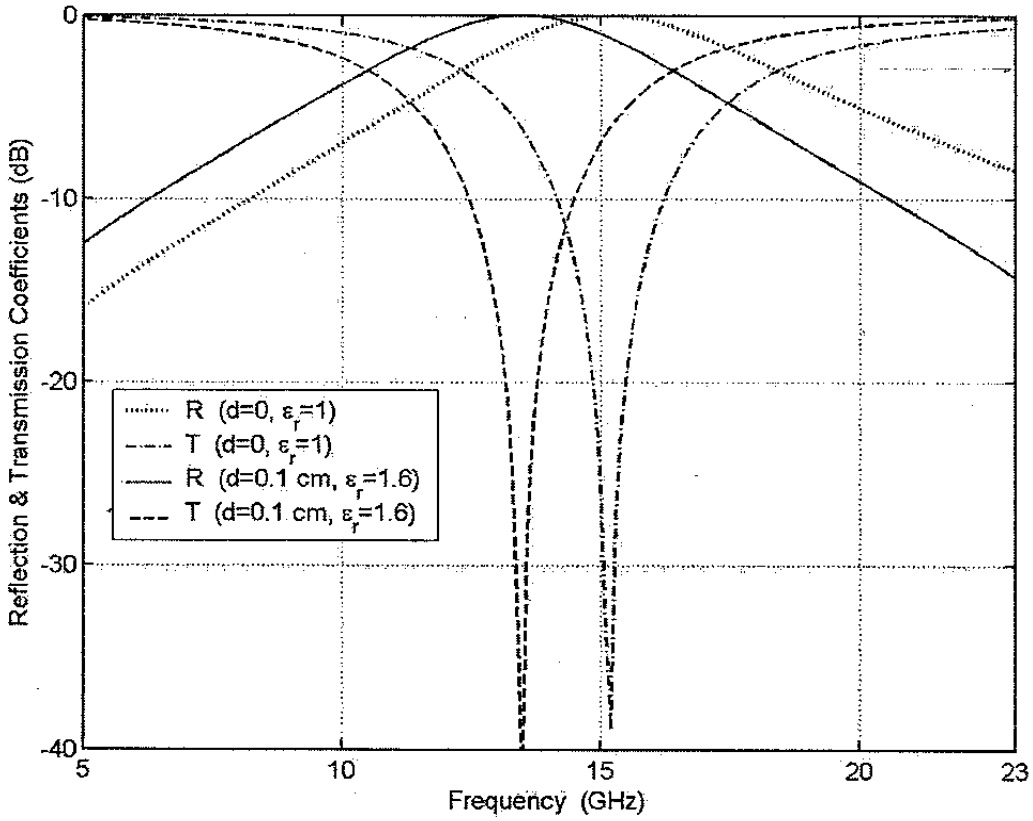

(a)

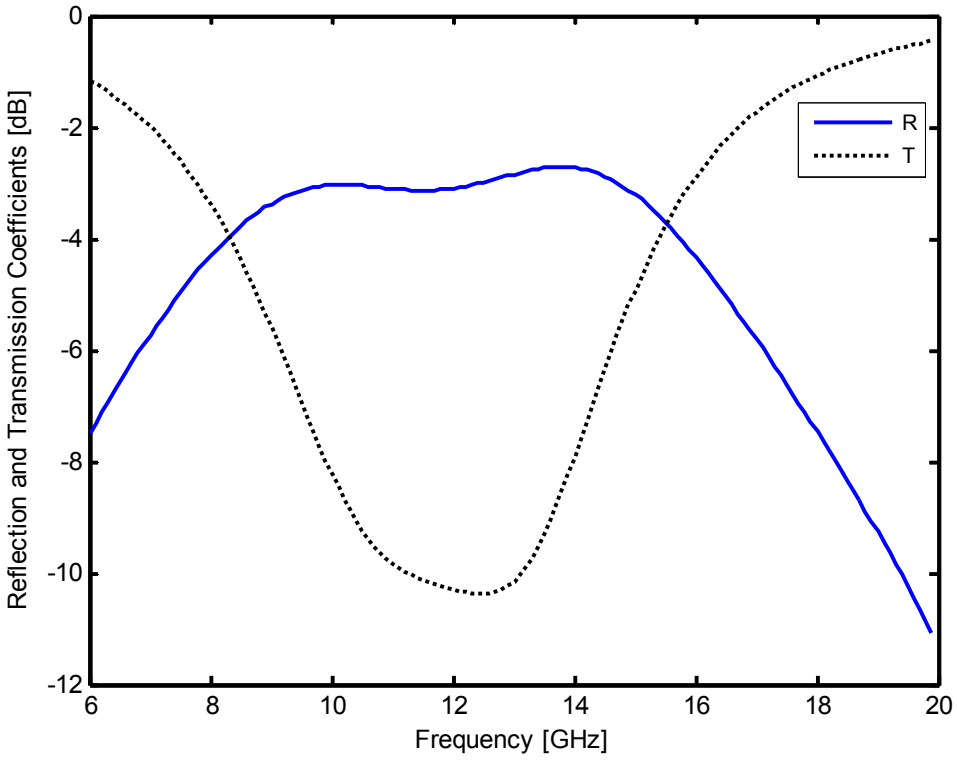

(b)

Figure 3.10 Reflection and transmission coefficients for dielectric backed L-dipole FSS at normally incident plane waves (a) taken from [14], page 20, Figure 1.7) (b) our analysis.

Since we employ piecewise triangular basis functions in our formulation and since piecewise sinusoidal basis functions were used in [14] one therefore expected almost identical results in both cases. The discrepancy between the current distributions is also obvious as can be seen in Figures 3.11a and 3.11b.

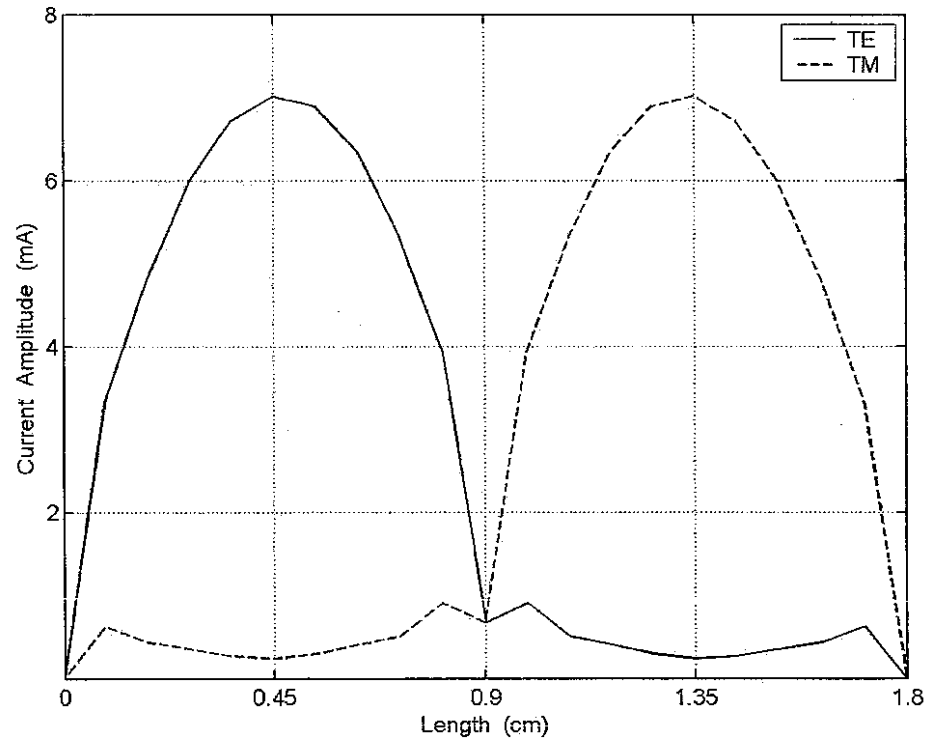

(a)

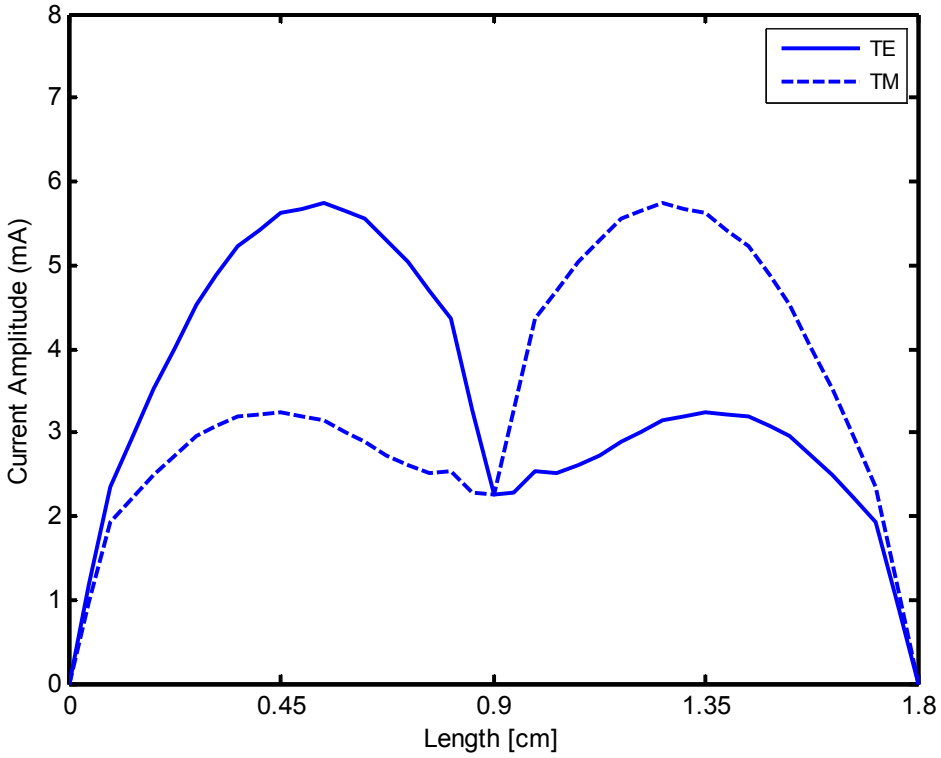

(b)

Figure 3.11 Current distributions versus length for dielectric backed L-dipole FSS (a) taken from [14], page 21, Figure 1.8) (b) our analysis

To find out the cause of this discrepancy we went through a detailed investigation of our formulation and found out that in [14] a sign error has been made in calculating the inner products. In [14] current is assumed to be flowing from the center point (corner) towards the end points whereas it should be flowing from one end of the L towards the other end, passing through the corner point as employed in our analysis. If this sign error is corrected then both formulations yield identical results for the current flowing in the L-shaped conductor, as given in Figure 3.11b.

3.3.3 FSSs with L-shaped apertures

Due to the major differences between our results and the results given in [14] at the early stages of our research, we searched the literature to see if we can compare our results with any other independent study. In [15], experimental results for an FSS formed from an infinite metal screen which has been periodically perforated by L-shaped apertures as shown in Figure 3.12.

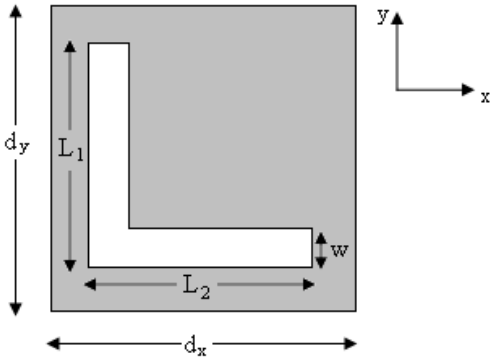

Figure 3.12 Frequency Selective Surface with L-shape aperture

For an FSS comprising of apertures, the concept of duality holds and hence, based on the basis of Babinet's principle [19] one can replace E with H and ε_o with μ_o in the solutions. For this reason, aperture and patch structures give complementary frequency responses. This means that, if a screen comprising of metal patches is totally reflective at some resonant frequency then the complementary structure which is formed by perforating a metallic screen with apertures (same shapes as patches) is totally transparent at the same frequency. Hence, in order to compare our work with the results given for the structure suggested in [15], we should compare our

reflection characteristics with their transmission characteristics. The theoretical reflection coefficient computed using our formulation and the theoretical/experimental results quoted in [15] are illustrated in Figure 3.13 for a structure where $L_1=L_2$ =1cm, w=0.1cm, $d_x=d_y$= 1.92cm, t=0 cm, and ε_r =1. The results are in good agreement as one takes into account that in our case the unknown current density is approximated by 19 piecewise triangular currents whereas in [15] the unknown aperture field of the L-shaped aperture is approximated using 6 waveguide modes. As it is seen in Figure 3.13, when the azimuth angle is -45° for a TM plane wave, resonance (transmission) occurs at 8.3GHz in [15] and 7.9GHz (reflection) in our study.

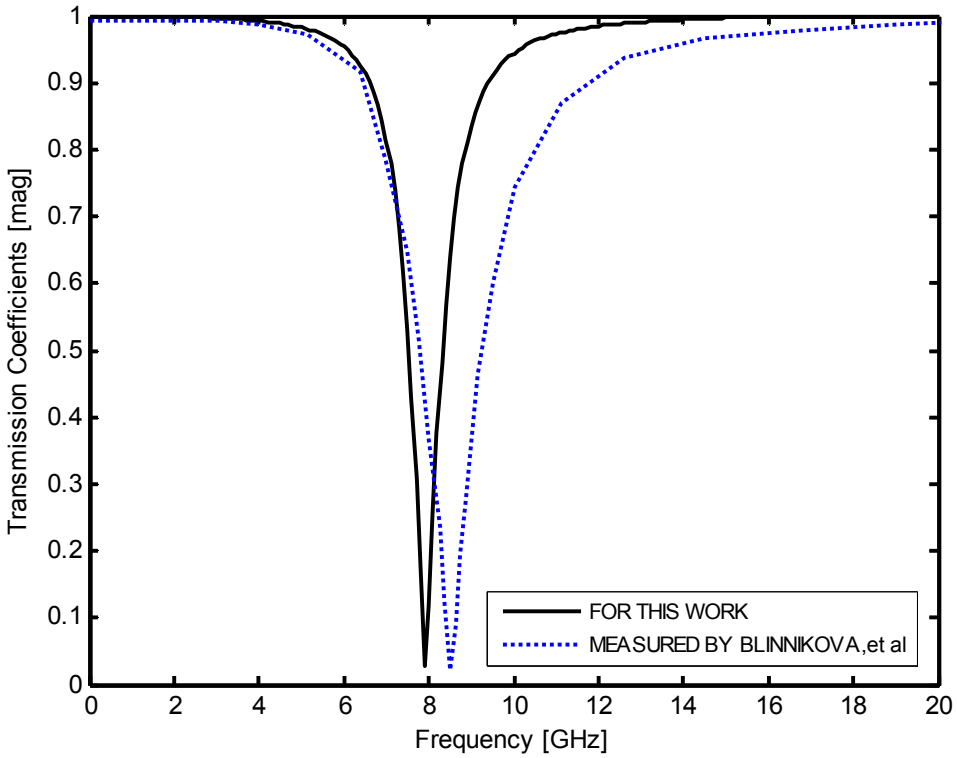

Figure 3.13 TM reflection coefficient for this work and TM transmission coefficient for Blinnikova, et al [15] versus frequency for freestanding L-shape structure FSS

On the other hand, Figure 3.14 displays the frequency response of FSS with L-shape dipole at different oblique incidences. As it is seen from the figure, there exists two resonance frequencies for a normally incident plane wave at 7.9GHz and 14GHz, respectively, but there is only one resonance occurs at 7.9GHz for an incident plane wave with an angle of $\phi = -45^{\circ}$.

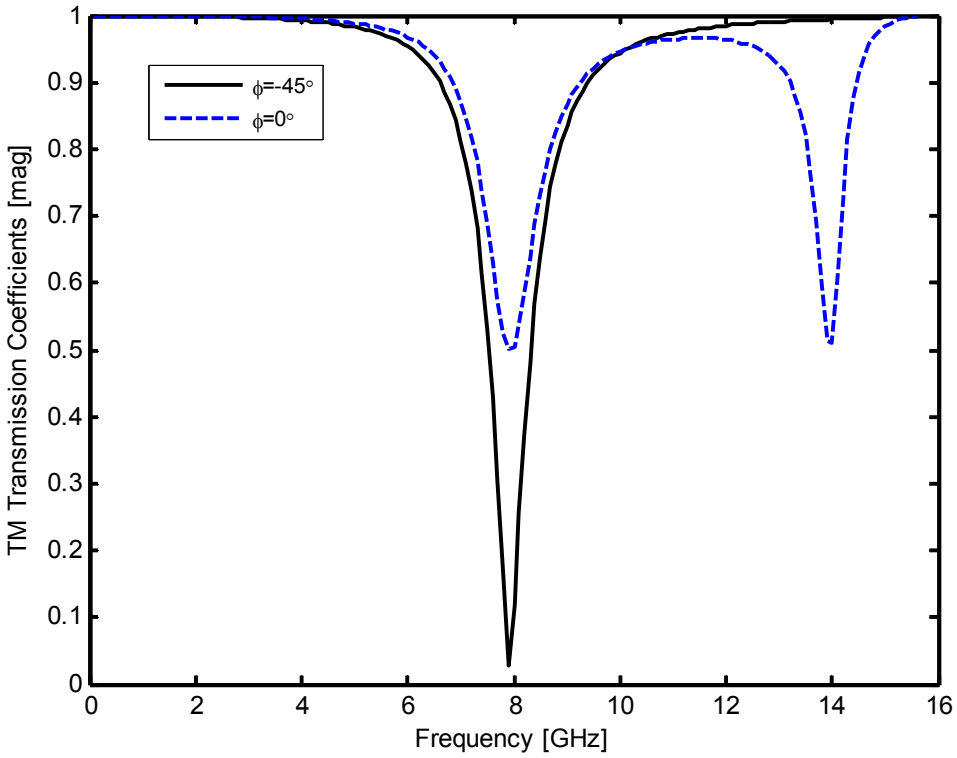

Figure 3.14 TM transmission coefficients versus frequency for a freestanding FSS with L-shape dipole at different oblique incidence angles

$L_1 = L_2 = 1cm, w = 0.1cm, t = 0cm, d_x = d_y = 1.92cm$

CHAPTER 4

NUMERICAL RESULTS

In this chapter, numerical results for the reflection and transmission characteristics of a triangular-shaped FSS are presented. Based on the analysis of Chapter 3, a computer program is generated to compute the reflection and transmission coefficients of triangular-shaped FSS as a function of frequency. The current distribution on the conducting elements can also be determined using the same program.

The geometry of a triangular element placed inside a square lattice having periodicities d_x and d_y in the x and y directions respectively is shown in Figure 4.1. As it is seen in the figure, length of the triangular conducting element is denoted by L and its width by w. The triangular shaped conducting elements are printed on a dielectric substrate with a thickness t and relative permittivity ε_r. In all our numerical computations, total number of induced currents on the conductor is taken to be 30 and 161 Floquet modes are used.

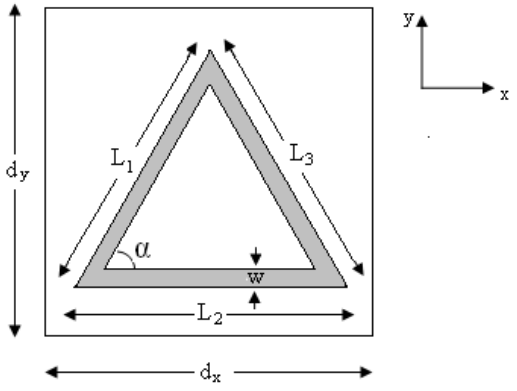

Figure 4.1 The geometry of triangular conducting element in a unit cell.

4.1 Numerical Results

In this section, first the current distribution on the triangular conducting element is provided. Then, reflection and transmission coefficients of TM and TE plane waves are given. Finally the influence of the parameters such as lattice dimensions, length and width of the conducting element, slab thickness, dielectric constant and the angle of incidence on the reflection and transmission characteristics are investigated over the frequency range of 4-16GHz. Between these frequencies only the first order modes propagate (i.e TM_{00} and TE_{00} Floquet modes) and no grating lobes exist.

In the computations for a FSS comprising of triangular shaped conductors, each arm length (L_1, L_2, L_3) and the width (w) of the conducting element are chosen as 0.94cm and 0.047cm, respectively. The inter-element spacing is $d_x=d_y=1$cm and slab thickness t is 0.5cm with $\varepsilon_r=2.3$. Furthermore, in all numerical computations 161 Floquet modes are used and each arm is divided into 10 segments. That is, a total of 30 piecewise triangular functions are used to approximate the current.

In Figure 4.2, for both freestanding and dielectric backed triangular-shaped FSS, TM and TE induced currents are plotted versus the length of the conductor. As seen in the figures, there is no difference between freestanding and dielectric backed structures in terms of the normalized current distribution. However, as it is seen in the figures, the resonance frequencies are quite different which is 13GHz for freestanding triangular-shaped FSS and 10.1 GHz for the dielectric backed triangular-shaped FSS.

In Figures 4.3a and 4.3b, magnitude of reflection and transmission coefficients is plotted versus frequency. Figure 4.3a displays that the TM waves at normal incidence are fully reflected at 13GHz for freestanding triangular-shaped FSS and 10.1GHz for dielectric backed triangular-shaped FSS. When the wave is TE polarized, the resonance frequencies shift to 13.6GHz and 10.5GHz for freestanding and dielectric backed triangular-shaped FSS, respectively.

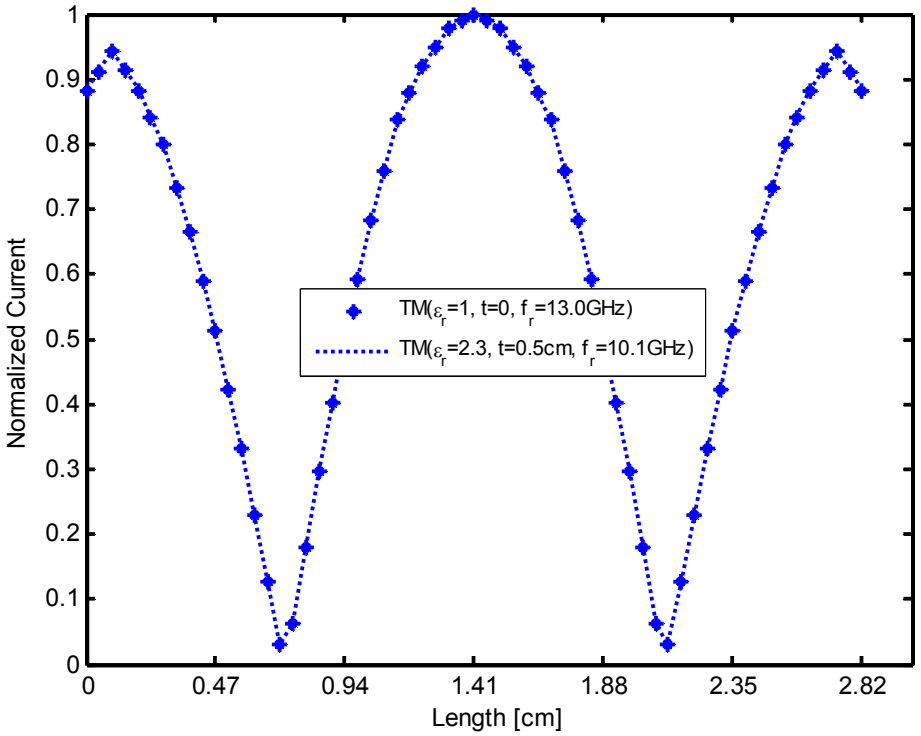

Figure 4.2a Normalized current versus length for the freestanding and dielectric backed triangular-shaped FSS at resonance frequency of TM incidence

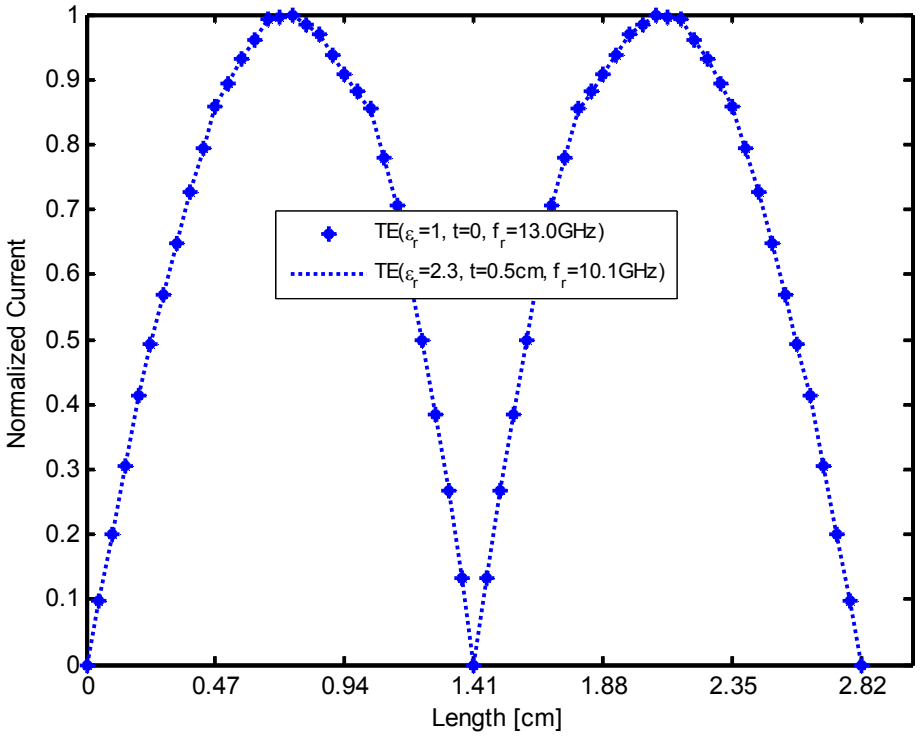

Figure 4.2b Normalized current versus length for the freestanding and dielectric backed triangular-shaped FSS at resonance frequency of TE incidence

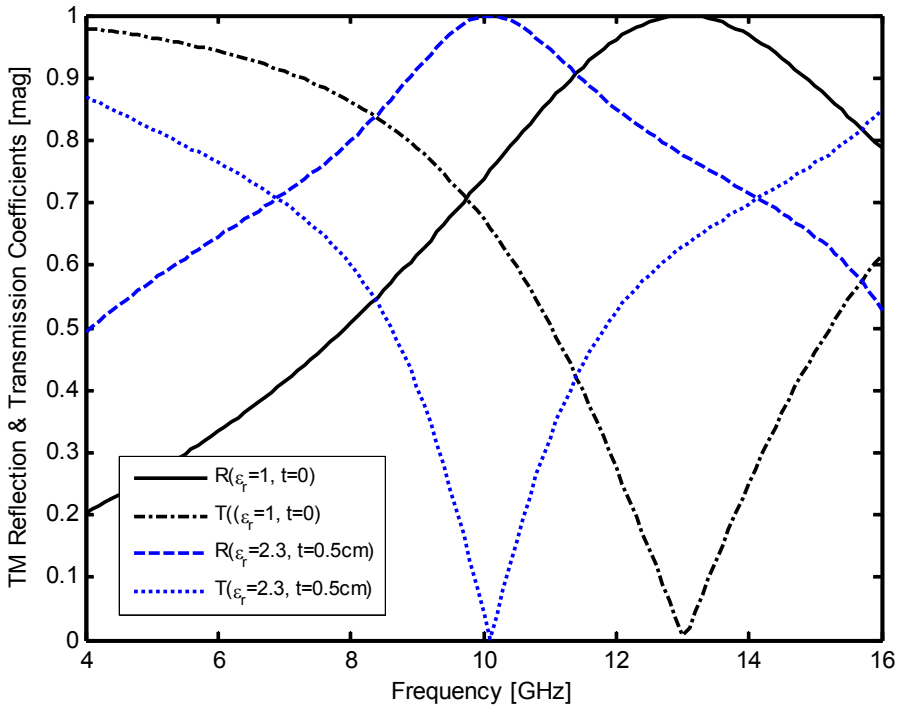

Figure 4.3a TM Reflection and Transmission Coefficients for the freestanding and dielectric backed triangular-shaped FSS for $\theta = \phi = 0^{\circ}$, d_x=d_y=1cm, L_1=L_2=L_3=0.94cm, w=0.047cm

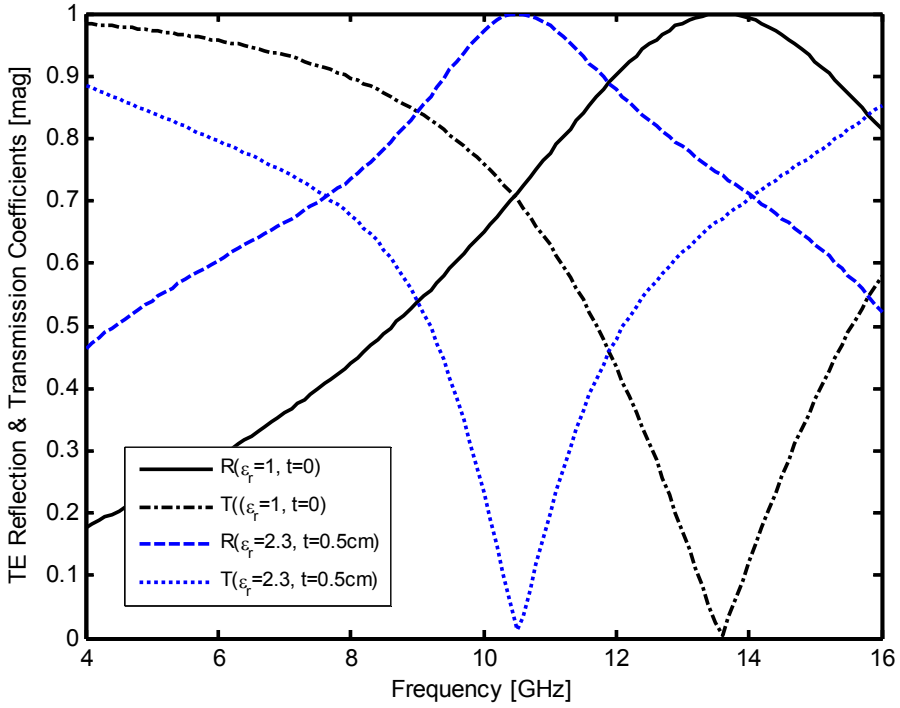

Figure 4.3b TE Reflection and Transmission Coefficients for the freestanding and dielectric backed triangular-shaped FSS for $\theta = \phi = 0^{\circ}$, d_x=d_y=1cm, L_1=L_2=L_3=0.94cm, w=0.047cm

The effects of changes in the parameters on the reflection coefficients are observed for both TM and TE incidence waves in the following figures. Figure 4.4 displays the effects of dielectric constant on reflection characteristics. So, when ε_r is increased, the resonant frequency decreases. At the same time a decrease in the bandwidth of the reflected wave is observed obviously while ε_r is increased.

For Figure 4.5, the reflection coefficient is plotted versus frequency for different slab thickness while the other parameters are unchanged. It is observed that the resonance frequency does not change when the slab thickness is increased or decreased for both TM and TE waves at normal incidence. Figure 4.6 illustrates the influence of lattice dimension on frequency response of the structure. If the dimensions of square lattice are increased while the size of triangular conductor is fixed, the resonance frequency for TM reflected wave increases. However, there is no change in resonance frequency for TE reflected wave. Moreover, for both types of polarization, the bandwidth of reflected wave decreases as the dimensions of square lattice increases. For this reason in order to decrease the resonance frequency, conducting elements should be printed tightly.

In Figure 4.7, reflection coefficients of TM and TE incidence waves are plotted with respect to the frequency for different lengths of triangular conducting element. If the length of one arm is decreased by 0.1cm and then by 0.2cm, the resonance frequency shifts to 11.7GHz and 13.5GHz, respectively. So we can say that the change in the length of conductor has same effect with the change in lattice dimensions while all other parameters are kept fixed. On the other hand, the bandwidth of reflected wave is wider for a larger triangular conductor. The other parameter that influences the frequency response is the width of triangular conducting element. Figure 4.8 displays the reflection coefficients against frequency for both TM and TE incidence waves for different widths of triangular conducting element. As it is seen, when the width of triangular conductor is increased from 0.01cm to 0.094cm, the resonance frequency shifts from 9.9GHz to 10.8GHz. In the last figure, Figure 4.9, effects of different incidence angles are observed. Although the angle of the incident wave is increased from 0 to 60°, the change in the resonant frequency is small. It shifts to the right by an amount of 0.3GHz for TM waves and shifts to the left with the same value for TE waves.

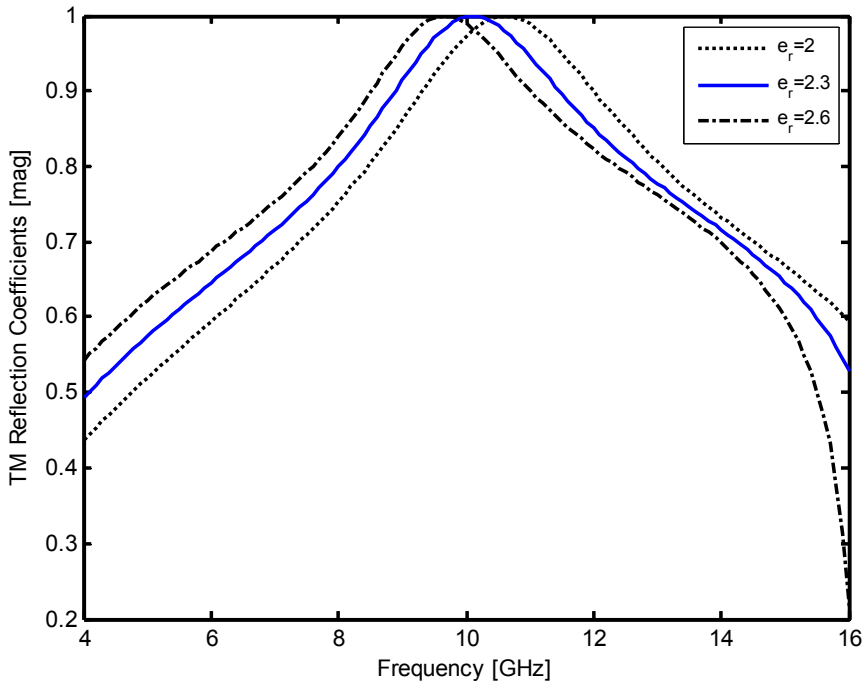

Figure 4.4a TM Reflection Coefficients versus frequency for triangular-shaped FSS at different values of ε_r ;

$\theta = \phi = 0^\circ, L_1 = L_2 = L_3 = 0.94cm, w = 0.047cm, d_x = d_y = 1cm, t = 0.5cm$

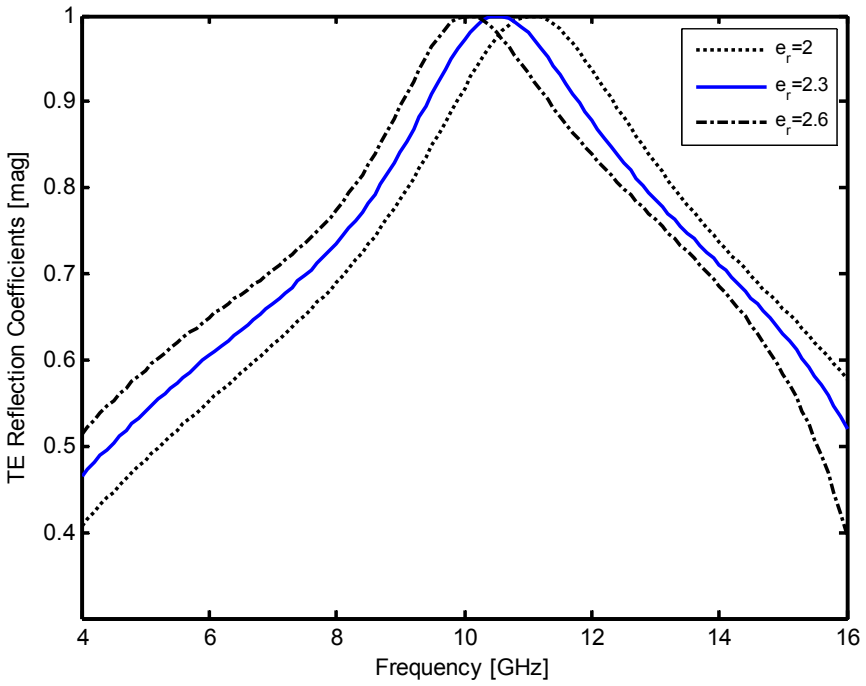

Figure 4.4b TE Reflection Coefficients versus frequency for triangular-shaped FSS at different values of ε_r ;

$\theta = \phi = 0^\circ, L_1 = L_2 = L_3 = 0.94cm, w = 0.047cm, d_x = d_y = 1cm, t = 0.5cm$

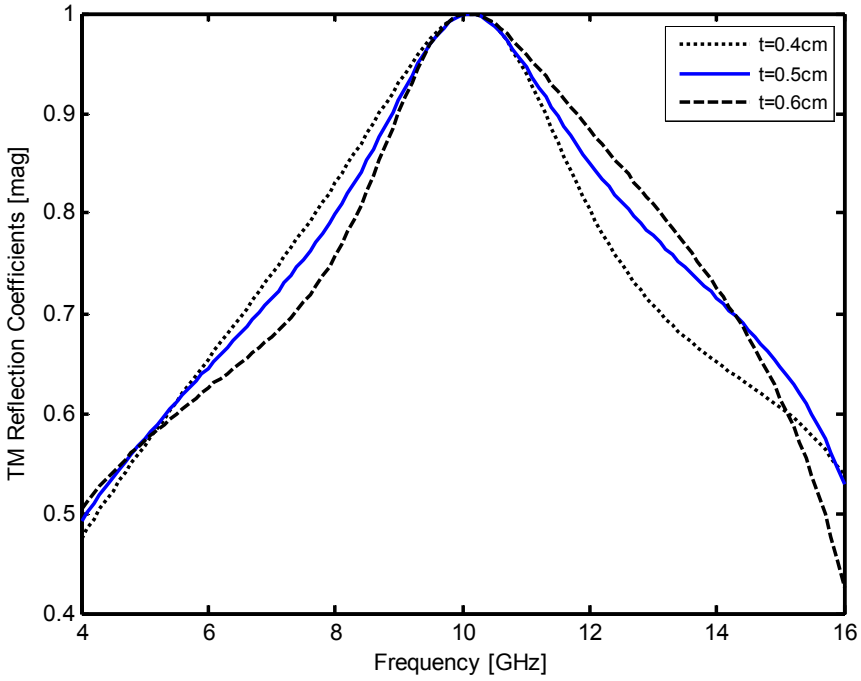

Figure 4.5a TM Reflection Coefficients versus frequency for triangular-shaped FSS at different slab-thicknesses;

$\theta = \phi = 0^{\circ}, \varepsilon_r = 2.3, L_1 = L_2 = L_3 = 0.94cm, w = 0.047cm, d_x = d_y = 1cm$

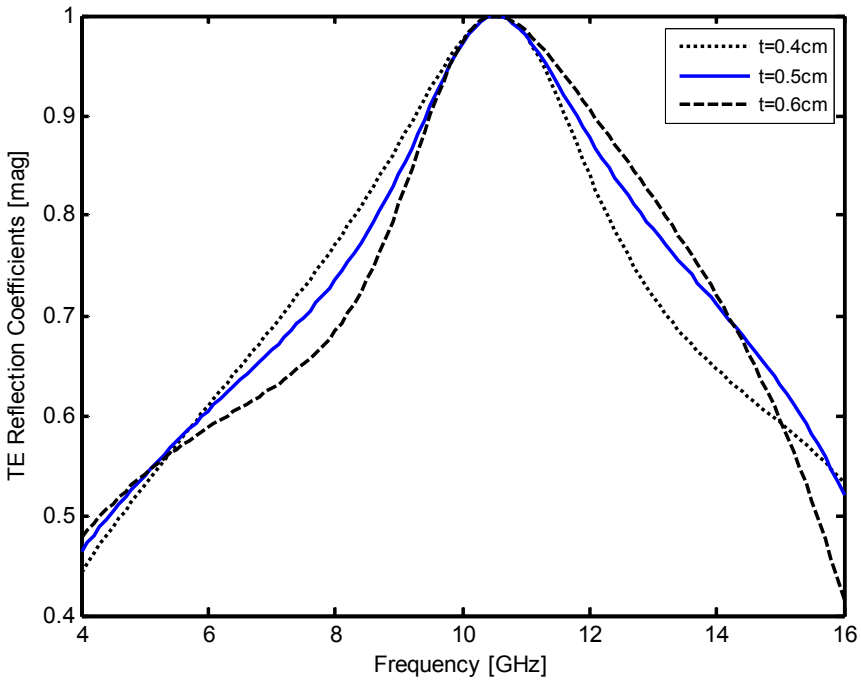

Figure 4.5b TE Reflection Coefficients versus frequency for triangular- shaped FSS at different slab-thicknesses;

$\theta = \phi = 0^{\circ}, \varepsilon_r = 2.3, L_1 = L_2 = L_3 = 0.94cm, w = 0.047cm, d_x = d_y = 1cm$

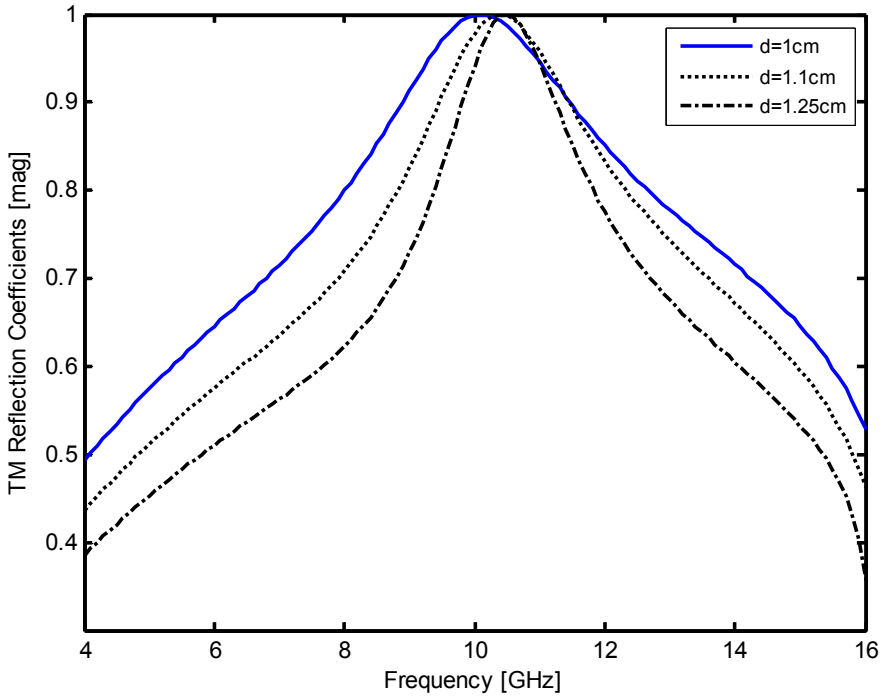

Figure 4.6a TM Reflection Coefficients versus frequency for triangular-shaped FSS at different lattice sizes; $\theta = \phi = 0^{\circ}, \varepsilon_r = 2.3, L_1 = L_2 = L_3 = 0.94cm, w = 0.047cm, t = 0.5cm$

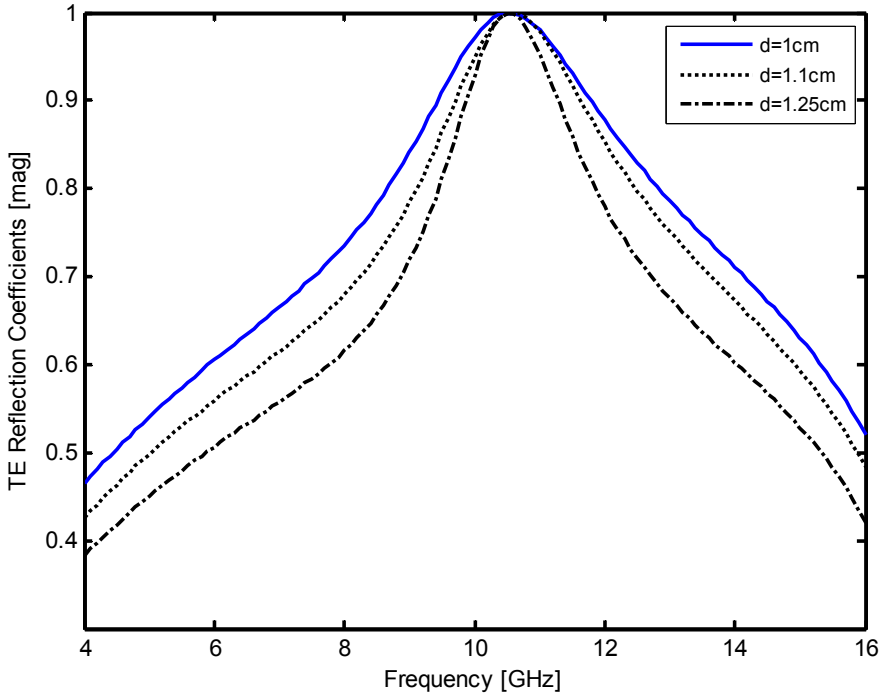

Figure 4.6b TE Reflection Coefficients versus frequency for triangular-shaped FSS at different lattice sizes; $\theta = \phi = 0^{\circ}, \varepsilon_r = 2.3, L_1 = L_2 = L_3 = 0.94cm, w = 0.047cm, t = 0.5cm$

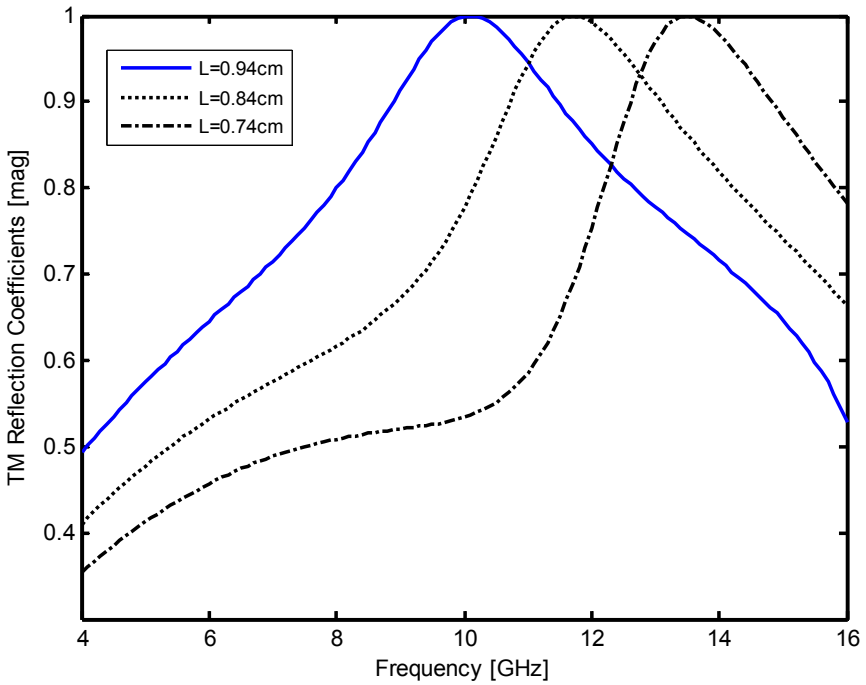

Figure 4.7a TM Reflection Coefficients versus frequency for triangular-shaped FSS at different lengths of conductor; $\theta = \phi = 0^{\circ}, \varepsilon_r = 2.3, w = 0.047cm, d_x = d_y = 1cm, t = 0.5cm$

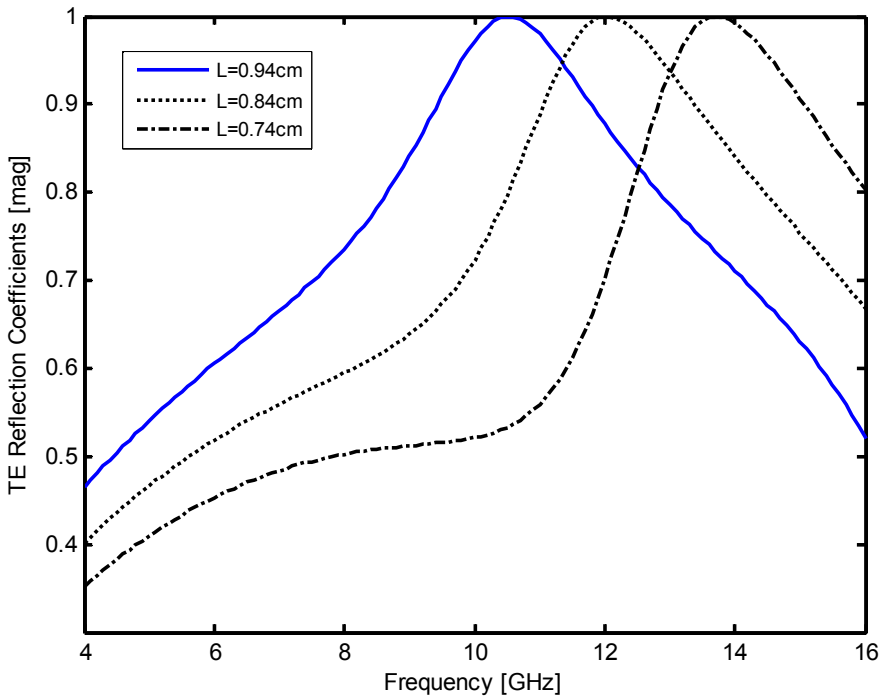

Figure 4.7b TE Reflection Coefficients versus frequency for triangular-shaped FSS at different lengths of conductor; $\theta = \phi = 0^{\circ}, \varepsilon_r = 2.3, w = 0.047cm, d_x = d_y = 1cm, t = 0.5cm$

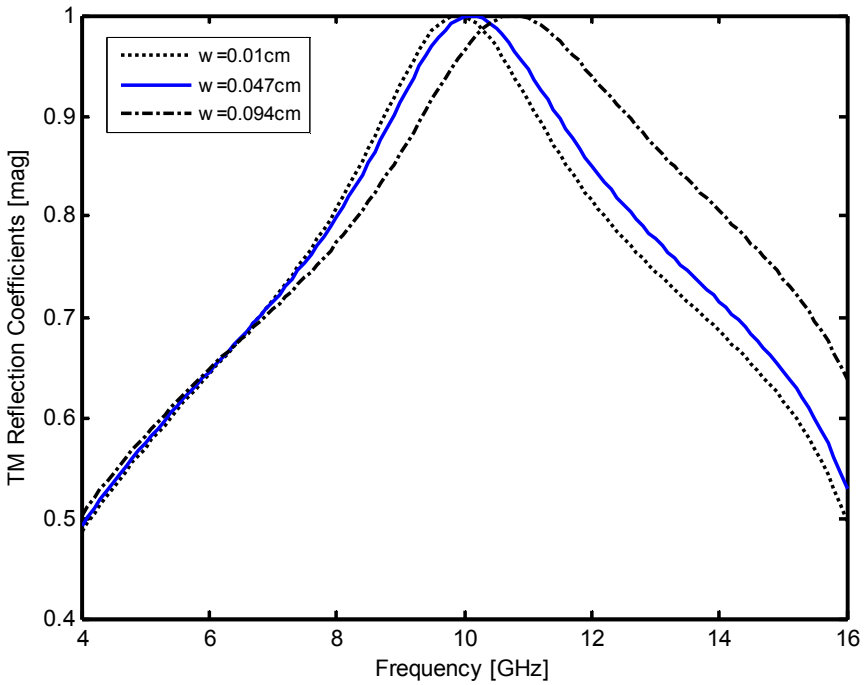

Figure 4.8a TM Reflection Coefficients versus frequency for triangular-shaped FSS at different widths of conductor;

$\theta = \phi = 0^{\circ}, \varepsilon_r = 2.3, L_1 = L_2 = L_3 = 0.94cm, d_x = d_y = 1cm, t = 0.5cm$

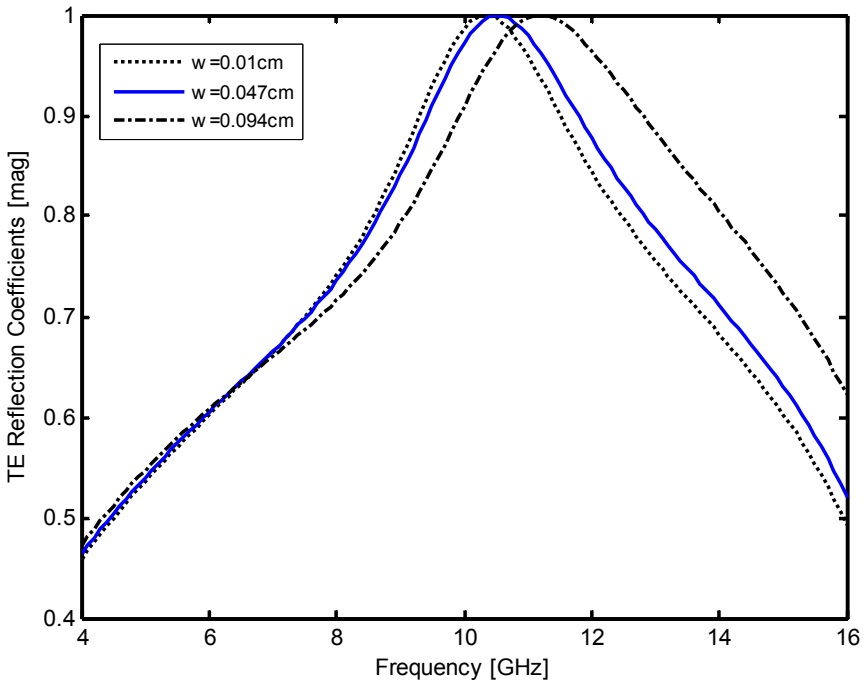

Figure 4.8b TE Reflection Coefficients versus frequency for triangular-shaped FSS at different widths of conductor;

$\theta = \phi = 0^{\circ}, \varepsilon_r = 2.3, L_1 = L_2 = L_3 = 0.94cm, d_x = d_y = 1cm, t = 0.5cm$

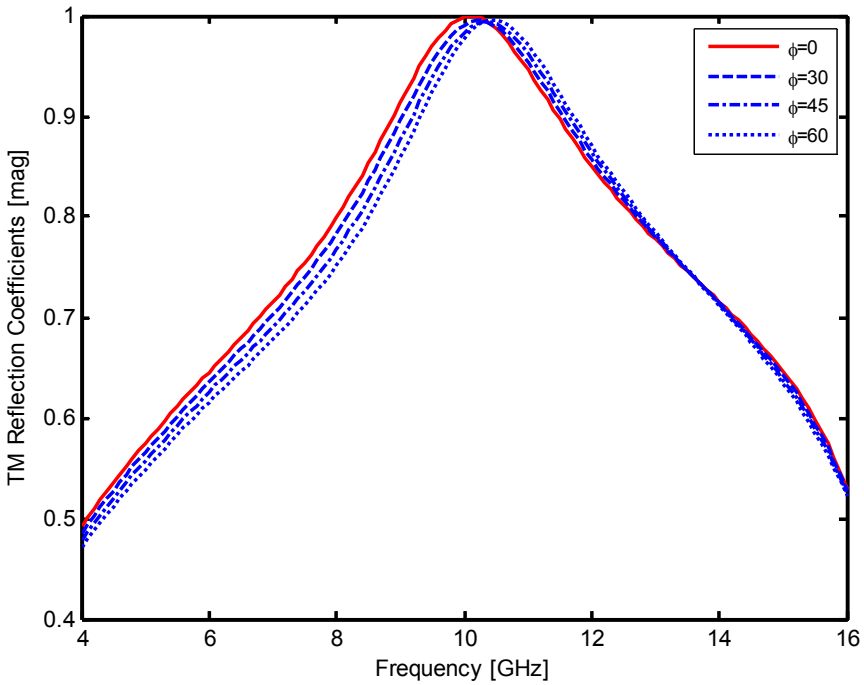

Figure 4.9a TM Reflection Coefficients versus frequency for triangular-shaped FSS at different oblique angle incidence;

$\theta = 0^{\circ}, \varepsilon_r = 2.3, L_1 = L_2 = L_3 = 0.94cm, w = 0.047cm, d_x = d_y = 1cm, t = 0.5cm$

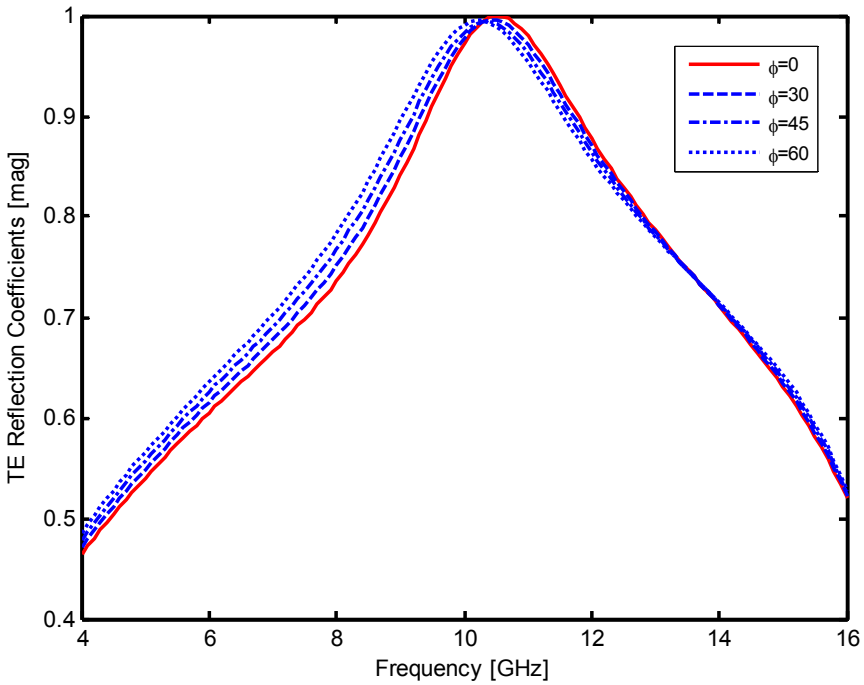

Figure 4.9b TE Reflection Coefficients versus frequency for triangular-shaped FSS at different oblique angle incidence;

$\theta = 0^{\circ}, \varepsilon_r = 2.3, L_1 = L_2 = L_3 = 0.94cm, w = 0.047cm, d_x = d_y = 1cm, t = 0.5cm$

4.2 Comparison of Concentric Ring FSSs with Triangular-Shaped FSSs

In order to analyze the frequency response of the concentric circular ring, a computer program is used which is developed for this type FSS structures. Then, for the comparison of concentric circular ring FSS with triangular shaped FSS, concentric circular ring is placed into a square lattice with the same lattice dimensions of triangular conducting element, $d_x=d_y=1$cm. Also, the inner radius and the outer radius of the concentric circular ring are chosen as 0.423cm and 0.47cm, respectively. On the other hand, each arm of the triangular conducting element is taken to be $r_{in}\sqrt{3}$ where r_{in} is the inner radius of the ring. Furthermore, for both structures width of the conducting elements are assumed to be 0.047cm and the slab thickness is taken as 0.5cm with a dielectric constant 2.3. Although the number of Floquet's modes is 161 for both structures, the number of basis functions is different from each other. For the concentric ring, basis functions are in sinusoidal form and for triangular conducting elements the basis functions are in piecewise triangular form with N equal to 30.

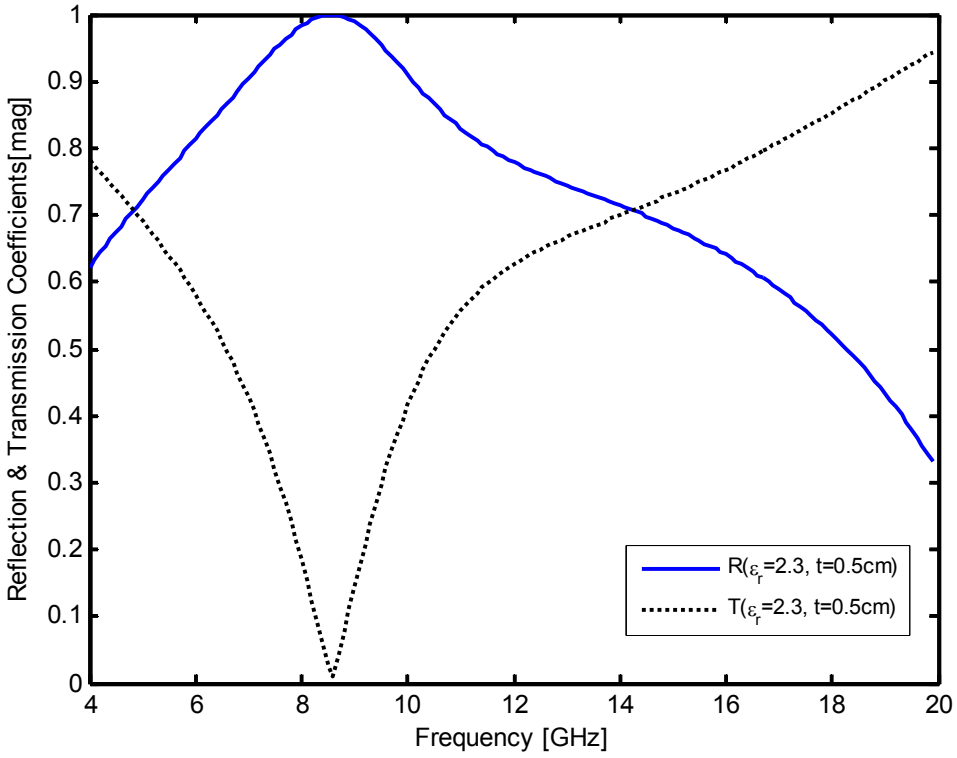

Figure 4.10 TM&TE Reflection and Transmission Coefficients versus frequency for the concentric circular ring FSS

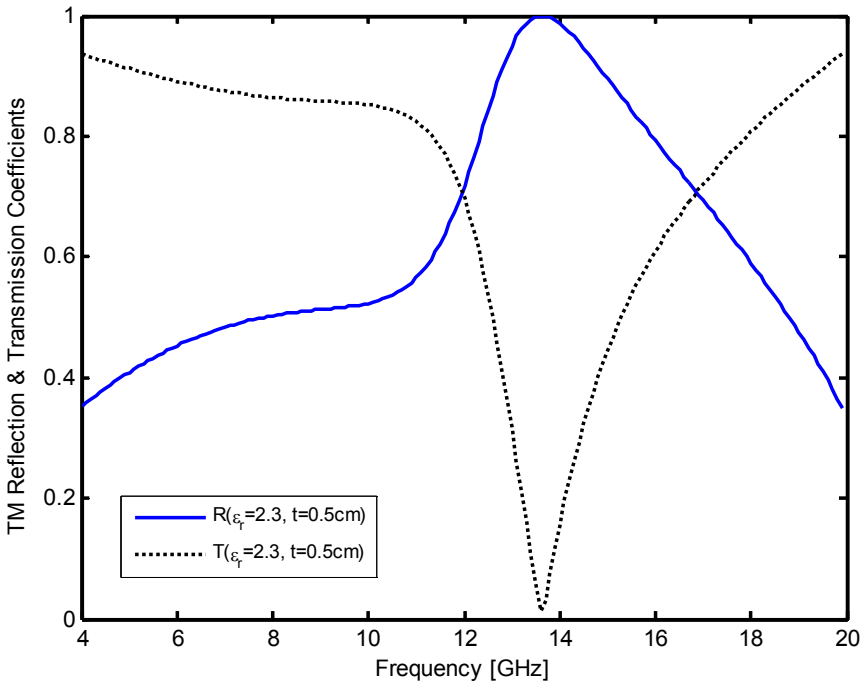

Figure 4.11a TM Reflection and Transmission Coefficients for dielectric backed triangular-shaped FSS; $\theta = \phi = 0^{\circ}, L_1 = L_2 = L_3 = 0.732cm, w = 0.047cm, \varepsilon_r = 2.3, t = 0.5cm, d_x = d_y = 1cm$

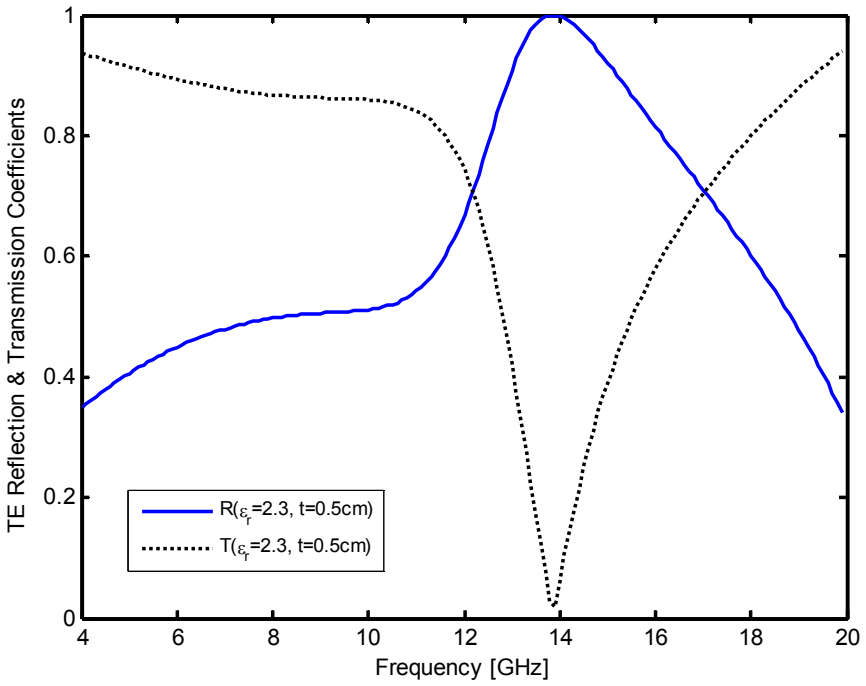

Figure 4.11b TE Reflection and Transmission Coefficients for dielectric backed triangular-shaped FSS; $\theta = \phi = 0^{\circ}, L_1 = L_2 = L_3 = 0.732cm, w = 0.047cm, \varepsilon_r = 2.3, t = 0.5cm, d_x = d_y = 1cm$

In Figures 4.10 and 4.11, the reflection and transmission coefficients of circular concentric ring and triangle-shaped FSS are plotted versus frequency, respectively. As it is seen, frequency responses of distinct geometries are different from each other. The reflection and transmission bandwidth of concentric circular ring FSS is also larger than the triangular conducting FSS. A concentric circular ring FSS has a resonance frequency at 8.6GHz both for TM and TE plane waves at normally incident. Due to the symmetry features of the circular ring, reflection and transmission coefficients are equal for all TM and TE plane waves at any incidence angles. However, full reflection and transmission occur at 13.6GHz for TM incident wave and 13.9GHz for TE incident wave for triangular conducting FSSs propagating at (0,0).

CHAPTER 5

CONCLUSION

In this thesis, FSS comprising of triangular conducting elements were analyzed to obtain the scattering properties of this structure.

In the analysis, the current induced on the conducting element is approximated by piecewise triangular currents with unknown coefficients. Then, using the method of moments the unknown current coefficients were determined and then used to determine the reflection and transmission coefficients.

In order to check the correctness of the algorithm developed for triangular conducting elements, numerical results obtained using this software for the structures comprising of strips and L-dipoles were compared with the experimental and theoretical results found in the literature. Once being sure of the validity of our software, results are obtained for FSSs comprising of triangular shaped conductors.

The variation of the reflection and the transmission characteristics with the conductor length, the width, the element spacing, the dielectric thickness, the dielectric constant and the angle of incidence are also examined.

For a triangular shaped FSS we can summarize our results as follows:

- When we increase ε_r, the frequency of total reflection decreases and shifts downward to the value of $f_o / \sqrt{(\varepsilon_r + 1)/2}$ where f_o is the freestanding resonance frequency.

- When the width of conductor is increased, the resonance frequency and the bandwidth also increase. Moreover, the width of conductor should have a value about L/10 in maximum. If it is greater than that value, some grating lobes will occur and it causes unwanted resonance frequencies.

- Slab thickness does not cause appreciable change in the resonance frequency and the reflection bandwidth.

- The effects of the length of conducting element are inversely proportional to the resonance frequency, but directly proportional to the bandwidth.

- However, lattice dimensions and the oblique angle have an opposite effect with respect to the length of the conductor. Because, when the lattice dimension is increased there is an increase in resonance frequency and a decrease in the bandwidth of reflection.

Hence, we can say that for a good FSS design, the conducting element should be small in terms of wavelength. Because the circumference of the metallic conductor defines the resonant frequency. Furthermore, if the inter-element spacing is kept as small as possible, the reflection bandwidth around the resonance can be increased and the structure is more stable to the increases in the incidence angle. Otherwise, for a large inter-element spacing early onset of grating modes occur. So, packing conducting elements tighter in the periodic cell delays the onset of grating modes.

Eventually, according to the numerical results and the reflection characteristics at resonance frequency, we can say that the FSSs with triangular conducting elements exhibit band-stop filter characteristics and fully reflect the energy in a specific frequency region.

This work can also be extended to look at the effects of chirality on a FSS comprising of triangular shaped elements.

Furthermore, this initial study may later be extended to analyze a metamaterial formed by cascading a triangular FSS to another FSS comprising of infinitely long thin conductors, as suggested in [20].

REFERENCES

[1] Constantine A. Balanis, (2008). *Modern Antenna Handbook.* John Wiley & Sons, Inc., Publication

[2] Mittra, R., Chan, C.H. and Cwik, T. (1988). Techniques For Analyzing Frequency Selective Surfaces - A Review. *IEEE Proceedings*, **76**, 12, 1593-1615

[3] Munk Ben A., (2000). *Frequency Selective Surfaces: Theory and Design.* John Wiley & Sons, Inc., Publication

[4] Ott, R.H., Kouyoumjian, R.G. and Peters, J. (1967). Scattering By a Two Dimensional Periodic Array of Narrow Plates. *Radio Sci.,* **2**, 1347-1349

[5] Keiburtz, R.B. and Ishimaru, A. (1961). Scattering By a Periodically Apperattured Conducting Screen. *IEEE Transactions on Antennas and Propagation,* AP,**3**, 506-544

[6] Chen, C.C. (1969). Scattering By a Two-Dimensional Periodic Array of Conducting Plates. *IEEE Transactions on Antennas and Propagation,* AP**,18,** 660-665

[7] Montgomery, J.P.(1975). Scattering By an Infinite Periodic Array of Thin Conductors on a Dielectric Sheet. *IEEE Transactions on Antennas and Propagation,* AP**,23,** 70-75

[8] Pelton, Edward L. and Munk B.A. (1979). Scattering From Periodic Arrays of Crossed Dipoles. *IEEE Transactions on Antennas and Propagation,* AP**,27,** 323-330

[9] Parker, E:A. and Hamdy S.M.A. (1981). Rings as Elements For Frequency Selective Surfaces *Electronics letters ,* **17**, 612-614

[10] Tsao, C.H. and Mittra,R. (1982). A Spectral- Iteration Approach For Analyzing Scattering From FSS's. . *IEEE Transactions on Antennas and Propagation,* AP**,30,** 303-308

[11] Tsao, C.H. and Mittra,R. (1984). Spectral domain analysis of frequency selective surfaces comprised of periodic arrays of cross dipoles and Jerusalem crosses. *IEEE Transactions on Antennas and Propagation,* AP**,32**, 478-486

[12] Pelton, E. L., and Munk, B. A.(1974). A Streamlined Metallic Radome. *IEEE Transactions on Antennas and Propagation,* AP**,22**, 799-803

[13] Vardaxoglou, J. C. and Parker, E. A.(1983). Performance of Two Tripole Arrays As Frequency-Selectıve Surfaces. *Electronics letters ,* **19**, 709-710

[14] Delihacıoğlu, K. (2007). *Analysis of Square Spirals On Planar Dielectric And Chiral Slabs.* Ph.D.Dissertation, University of Gaziantep,Turkey.

[15] Blinnikova, O.A., Don,N,G. and Kirilenko,A.A.(2007). Frequency Selective Surfaces with L-Shaped Apertures. *International conference on antenna theory and techniques,* 149-151

[16]Harrington, Roger F.(1967). Matrix Methods for Field Problems. *Proc. IEEE,* **55**, 136-149

[17] Bhattachharyya, Arun K. (2006). *Phased Array Antennas* . John Wiley & Sons, Inc., Publication

[18] Amitay, N., Galindo, V. and Wu, Chen P. (1972).*Theory And Analysis of Phased Array Antennas.* John Wiley & Sons, Inc., Publication

[19] Constantine A. Balanis, (1997). *Antenna Theory: Analysis And Design.* John Wiley & Sons, Inc., Publication

[20] Sabah, C. (2008). *Analysis, application and a novel design of double negative metamaterials*. Ph. D. Dissertation, University of Gaziantep, Gaziantep, Turkey